Directional solidification at high speed. II. Transition to chaos

Klaus Kassner,[1] Chaouqi Misbah,[2,*] Heiner Müller-Krumbhaar,[1] and Alexandre Valance[2,*]

[1]*Institut für Festkörperforschung des Forschungszentrums Jülich, 52425 Jülich, Germany*

[2]*Institut Laue-Langevin, Boîte Postale 156, 38042 Grenoble Cedex 09, France*

(Received 11 November 1993; revised manuscript received 17 February 1994)

This paper continues our analysis of various aspects of interface dynamics in rapid solidification. The description is based on a local continuum model, relevant to both liquid crystals and conventional materials. It was derived in a preceding paper, where we dealt with primary and secondary instabilities evolving from an initially flat interface when the control parameter, a renormalized temperature gradient, is decreased. Here we focus on more complex dynamic states arising from the interaction of different oscillatory modes. We find quasiperiodic motion to occur when one of the oscillators is a (parity-breaking) drifting mode. Quasiperiodicity precedes a transition to chaos, the route to which we describe in some detail. The absence or manifestation of mode locking as well as other interesting dynamic states are discussed. A second quasiperiodic scenario, where the control parameter is the wave number of the pattern, provides evidence that the transition to chaos via intermediate quasiperiodic states is generic for systems that possess the drift instability. Both chaotic regimes are briefly characterized, and Lyapunov exponents are computed for a variety of states. We find that all chaotic states have two vanishing Lyapunov exponents, a feature that we explain as a consequence of translational invariance. An implication is that the Lyapunov dimension of chaotic attractors exceeds three. Moreover, we find attractors whose dimension is larger than four. All the considered chaotic states are purely temporal. An outlook is given on interesting and important questions related to the long-time behavior of our model on large length scales, where spatiotemporal chaos is to be expected.

PACS number(s): 61.50.Cj, 81.30.Fb, 05.70.Fh

I. INTRODUCTION

The physical aspects of directional solidification that are pertinent to this work have been discussed in the preceding companion paper [1], henceforth referred to as I. Therefore, we may immediately proceed to the plan of the present paper.

In Sec. II, we recall the basic local equation of motion derived in I and discuss some of its implications. This includes a consideration of the dispersion relation and its probable consequences for the large-scale behavior of the system, and a discussion of oscillatory planar front solutions. Their existence will be important in Sec. III, where we give a detailed account of the quasiperiodic transition to chaos, a brief description of which has been presented in our earlier work [2]. Furthermore, in support of the claimed genericity of the described scenario, we give a description of another path in parameter space also leading to chaos via quasiperiodicity. This second path has so far only been considered in the framework of a two-mode approximation [3]. Mode-locking states are considered briefly. Section IV deals with states inside the chaotic regime. We characterize them by calculating their Lyapunov exponents and discuss the influence of translational invariance on the complexity of the strange attractor. Finally, we summarize our results in Sec. V. Two appendices give details of numerical methods.

II. LOCAL DESCRIPTION

In I, extensive arguments were given on the basis of symmetry and scaling considerations about what the evolution equation of the model must look like in the vicinity of the upper absolute stability limit.

All that remains to be done then is to determine the numerical values of the coefficients of that equation. These have been derived for the one-sided model [4,5], for the symmetric model [6], and now also for the general two-sided case [7]. The derivation is based on a singular expansion about the critical point corresponding to absolute stability; details may be found in Ref. [8].

In its most general form, the resulting local equation reads

$$\zeta_{TT} - \left[2 + \frac{1}{k} + v\right]\nabla^2\zeta_T + \left[1 + \frac{1}{k} + v^2\right]\nabla^4\zeta + 8k\nabla^2\zeta + 8kl_T^{-1}\zeta$$

$$= 2\zeta_T\nabla^2\zeta + 2(|\nabla\zeta|^2)_T - 2\nabla^2(|\nabla\zeta|^2) - 2v(\nabla\zeta)\nabla(\nabla^2\zeta) - \frac{2}{k}\nabla[(\nabla\zeta)\nabla^2\zeta] - 2\nabla[(\nabla\zeta)|\nabla\zeta|^2] . \quad (2.1)$$

*Present address: Laboratoire de Spectrométrie Physique, Université Joseph Fourier, 38402 Saint-Martin-d'Hères Cedex, France.

Herein ζ denotes the position coordinate of the interface along the direction defined by the thermal gradient. Subscripts T indicate derivatives with respect to the slow time variable $T = \epsilon t$, and ∇ is a $d-1$ dimensional gradient operator with respect to the slow coordinate(s) $X = \sqrt{\epsilon} x (Y = \sqrt{\epsilon} y)$ perpendicular to the gradient direction (d is the bulk dimension of the system considered). In the two-dimensional case, to which we will restrict ourselves here, we simply have $\nabla = \partial / \partial X$. The small parameter ϵ measures the distance of the system from the absolute stability limit, and is given by

$$\epsilon = \frac{1}{2k} - \frac{d_0}{l} , \qquad (2.2)$$

where

$$d_0 = \frac{\gamma T_M}{Lm\Delta c} \qquad (2.3)$$

and

$$l = \frac{2D}{V} \qquad (2.4)$$

are the physical capillary and diffusion lengths, respectively. γ is the—isotropic—surface tension, T_M the bulk melting temperature of the pure solid, m the absolute value of the liquidus slope, L the latent heat per unit volume, and D the diffusivity in the liquid phase.

Solutions to Eq. (2.1) constitute a zeroth order in ϵ asymptotic approximation to the interface position arising in the full model [8].

The equation depends on the three parameters l_T^{-1}, ν, and k. The most important of these is l_T^{-1}, given by

$$\frac{l}{\tilde{l}_T} = l_T^{-1} \epsilon^2 , \qquad (2.5)$$

where

$$\tilde{l}_T = \frac{m\Delta c}{G} \qquad (2.6)$$

is the (physical) thermal length. The notation for this parameter emphasizes its relationship with the reduced inverse thermal length. This would suggest $l_T^{-1} \propto G/V$, which is indeed true for a *constant* distance ϵ from the threshold. However, in experiments it is *not* ϵ that is fixed but rather the material parameters. Now ϵ contains its own velocity dependence:

$$\epsilon = \frac{\gamma T_M}{2mL\Delta cD}(V_a - V) , \qquad (2.7)$$

where $V_a = mL\Delta c/\gamma T_M k$ is the velocity that corresponds to the absolute stability limit. Therefore, we have

$$l_T^{-1} \propto \frac{G}{V(V_a - V)^2} , \qquad (2.8)$$

and it is easy to verify that, for given material parameters, $\partial l_T^{-1}/\partial V > 0$ at velocities below and close to V_a, as must be the case. Therefore, l_T^{-1} is a renormalized temperature gradient, which is proportional to the physical gradient but has a relatively complicated velocity dependence.

The second parameter ν is the ratio of diffusivities in the solid and liquid phases: $\nu = D_s/D$. Hence $\nu = 0$ for the one-sided model, and $\nu = 1$ for the symmetric model. For $\nu = 0$, the function $\zeta(X) = \ln(|X - X_0|)$ asymptotically solves the stationary equation for $X \to X_0$. This means that in the one-sided model there may exist solutions with infinitely deep cusps, whereas for finite ν the minima of the profile remain finite. Indeed, we have encountered states with a tendency to develop deep cusps as ν becomes small (which greatly impedes the numerical solution). The existence of stationary solutions of this type has been discussed in I.

Our final parameter is the segregation coefficient k which has been set equal to one throughout this study. At least for liquid-crystal systems, this is expected to be a good approximation [9,10].

A. Dispersion relation and neutral curve

Equation (2.1) is solved by $\zeta(X) \equiv 0$, the usual planar front solution of directional solidification. Because our equation is second order in time, a linear stability analysis of this solution leads to a dispersion relation with two branches. From

$$\omega^2 + \left[2 + \frac{1}{k} + \nu\right]\omega q^2 + \left[1 + \frac{1}{k} + \nu^2\right]q^4$$
$$- 8kq^2 + 8kl_T^{-1} = 0 , \qquad (2.9)$$

we find immediately

$$\omega_{1/2} = -\left[1 + \frac{1}{2k} + \frac{\nu}{2}\right]q^2$$
$$\pm \left\{\left[\left[1 + \frac{1}{2k} + \frac{\nu}{2}\right]^2 - \left[1 + \frac{1}{k} + \nu^2\right]\right]q^4 \right.$$
$$\left. + 8kq^2 - 8kl_T^{-1}\right\}^{1/2} . \qquad (2.10)$$

Only the upper branch can have a positive real part leading to instability of the planar front solution. An example is shown in Fig. 1. Note that Eq. (3.1) of I reduces to the symmetric-model version of Eq. (2.9), if the appropriate scalings are inserted $[\omega \to \epsilon\omega, q^2 \to \epsilon q^2, \tilde{l}_T^{-1} \to \epsilon^2 l_T^{-1}$, and Eq. (2.2)], and the expansion is truncated at order ϵ^2.

This dispersion relation is different in two important respects from that of a related and well-investigated equation, the Kuramoto-Sivashinsky equation, which appears, for example, in a similar asymptotic analysis of *free growth* at large undercooling, when a kinetic coefficient is taken into account [11]. First, the band of unstable wave numbers does not normally extend down to $q = 0$; second, there is a nonzero imaginary part at $q = 0$. This may have important consequences for the large-scale long-time behavior of our equation, which should be dominated by wave numbers in the vicinity of $q = 0$. As for the Kuramoto-Sivashinsky equation, there is strong evidence [12] that the scaling of the interface width is the same as that of a stochastic equation, the well-known Kardar-Parisi-Zhang equation [13]. In our equation, both the dispersion relation and the fact that all nonlinearities are
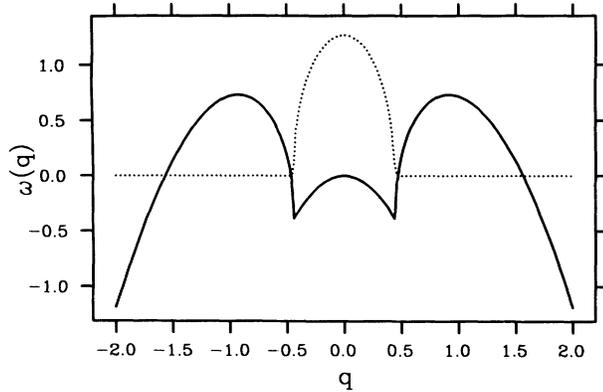
FIG. 1. Upper branch of the dispersion relation obtained by linear stability analysis of the planar front. Solid line: real part; dashed line: imaginary part. Parameters: $l_T^{-1}=0.2$, $v=1$, and $k=1$ (symmetric model).

irrelevant (according to power-counting arguments) point to a probably different behavior. This is an interesting research problem that we hope to address in the future.

Differentiating Eq. (2.9) with respect to q, and setting both $\omega=0$ and $\partial\omega/\partial q=0$, we obtain the critical point describing the absolute stability limit:

$$q_c^2=\frac{4k^2}{1+k+kv^2}, \quad l_{Tc}^{-1}=\tfrac{1}{2}q_c^2 . \tag{2.11}$$

Figure 2 provides an example for the general appearance of the neutral curve obtained from (2.9) by setting $\omega=0$ and solving for l_T^{-1}.

Below a certain value of l_T^{-1}, modes of wave numbers q and $2q$ are simultaneously unstable. This codimension-two point is given by $q^2=\tfrac{2}{5}q_c^2$, and $l_T^{-1}=\tfrac{16}{25}l_{Tc}^{-1}$. In the
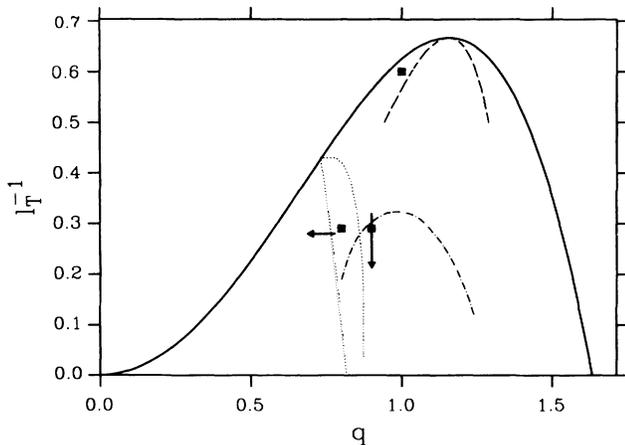

FIG. 2. The interesting part of parameter space for the symmetric model. Schematic representation of the Eckhaus boundary (dashed line), the bifurcation lines for period halving and parity breaking (dotted lines), and the VB instability (dash-dotted line). The squares indicate points, where one of the three oscillators discussed in the text is realized in pure form. The arrow that points downward indicates the path corresponding to the chaotic scenario described in Sec. III B. The arrow pointing to the left shows the path corresponding to the scenario of Sec. III C.

the symmetric model, $q\approx0.730$ and $l_T^{-1}\approx0.427$; in the one-sided model, $q\approx0.894$ and $l_T^{-1}=0.64$.

B. Nonstationary planar solutions

The behavior of the dispersion relation at $q=0$ suggests immediately that in addition to the *stationary* planar front, there are *oscillatory* planar solutions. This can be seen by dropping all spatial derivatives in Eq. (2.1), which yields

$$\zeta_{TT}+8kl_T^{-1}\zeta=0 , \tag{2.12}$$

the solutions of which are, of course, simple temporal oscillations

$$\zeta(T)=A\cos(\bar\omega T-\phi), \quad \bar\omega=\sqrt{8kl_T^{-1}} . \tag{2.13}$$

It is easy to check that these oscillatory states are *not* exact solutions to the full model. Indeed, if we expand the full dispersion relation [Eq. (2.8) of I] beyond order ϵ^2, we obtain, for $q=0$,

$$\omega=\pm i\epsilon\sqrt{8kl_T^{-1}}-\epsilon^2[1+k(v+2)]l_T^{-1} , \tag{2.14}$$

which shows that the oscillation is damped. Nevertheless, these oscillatory states should not be considered mere artifacts of the asymptotic expansion, because Eq. (2.14) also shows that the damping goes to zero faster than the oscillation frequency when ϵ is sent to zero. Thus these states become more long lived as ϵ becomes smaller and, in fact, physically more important.

These solutions might be a useful starting point for an explanation of structures consisting of alternating bands of planar front and dendritic morphologies which are observed in rapid solidification experiments [14–16]. In a real system, the parameter l_T^{-1} will vary when the velocity oscillates, because l_T^{-1} is normalized by the diffusion length, and in addition depends on the velocity via ϵ. This means that a system described in Eq. (2.13) might (for large enough amplitude A) actually fall, in its low-velocity half-period, below the critical value of l_T^{-1}, which would lead to the development of a cellular structure [or a dendritic one, which is not describable by Eq. (2.1)]. If the subsequent acceleration of the interface increased its velocity enough to drive l_T^{-1} beyond l_{Tc}^{-1}, the cells would have to flatten out into a planar interface again, and so on. The combination of the driving force during the nonplanar motion and the damping in the planar stage might well lead to limit-cycle behavior. At present, this is a hypothetical statement. Whether these oscillatory states are pertinent to banding or not has to be decided by more detailed research.

In view of the important work of Karma and Sarkissian [17], who have addressed this question, it seems likely that one must include kinetic effects such as solute trapping to arrive at a realistic description of banded structures.

III. QUASIPERIODICITY AND TRANSITION TO CHAOS

A. Interacting oscillators

In the companion paper, we identified the basic stationary states and secondary instabilities of the dynamic

KASSNER, MISBAH, MÜLLER-KRUMBHAAR, AND VALANCE

system defined by Eq. (2.1). Stationary states were obtained by a shooting method, and to investigate the time-dependent behavior the dynamical system was integrated starting from various types of initial conditions using Gear's backward difference method [18]. Details of the numerical procedure are given in Appendix A.

Three primary stationary growth modes were found [19], one consisting of axisymmetric cells, the other two broken-parity (BP) structures, one of which exhibits a lateral drift motion. Further secondary instabilities include a period-halving bifurcation, the Eckhaus instability, and an oscillatory instability leading to the vacillating-breathing (VB) mode.

It is advisable to be careful in distinguishing between oscillatory *instabilities* and oscillatory *states* or growth modes. Up to now, we have identified three prototypes of oscillatory states. These are the VB mode, a spatially homogeneous oscillation, and the drifting BP mode. It should be evident that whether the BP mode is considered stationary or oscillatory depends on the frame of reference. In the laboratory frame, any point with a fixed lateral coordinate oscillates up and down as it is passed by the wave form.

The VB mode arises via a Hopf bifurcation (see I); therefore the corresponding instability is definitely oscillatory.

For the homogeneous oscillation, the situation is more intricate. The growth rate of the Eckhaus instability is purely real, hence it cannot be considered oscillatory. Nevertheless, the dynamics of states created in the Eckhaus unstable region of parameter space above the codimension-two point are usually dominated by a homogeneous oscillation of the whole pattern [which is due to nonzero imaginary part at $q=0$ of dispersion relation (2.10)], until a stationary state is reached. The role of the Eckhaus instability here is only to keep the interface away from the unstable stationary state. For a large enough aspect ratio, the system will eventually manage to find a *stable* stationary state by wavelength adjustment, as was demonstrated in I. If the initial state is the unstable stationary state, and the only perturbation is numerical noise, this adjustment is possible without oscillations. Generically, however, i.e., for large enough perturbations, we find homogeneous oscillations which can become quite pronounced. Even though these are always damped, they may become physically important through the interaction with instabilities that drive them.

Finally, the BP mode also arises from a long-wavelength instability of the symmetric state. Again, the imaginary part of the growth rate is zero, so the bifurcation is not of Hopf type. Hence the instability is not oscillatory but the resulting state is, at least in a nonmoving frame of reference.

In Figs. 3–5, we give temporal power spectra of examples for each of the three aforementioned states, demonstrating their oscillatory nature. The points in parameter space corresponding to these examples are shown as squares in Fig. 2. These spectra were obtained by taking the Fourier transform of the position of a single interface point (with a fixed X coordinate). Each of them displays a dominant single frequency and its strongly damped
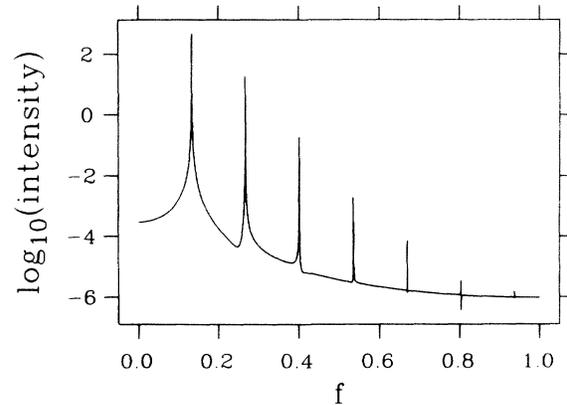

FIG. 3. Power spectrum of a pure VB mode. Logarithmic representation. The spectrum consists of a single frequency and a few (strongly damped) harmonics. Parameters: $l_T^{-1}=0.29$, $q=0.9$, and $v=1.0$.
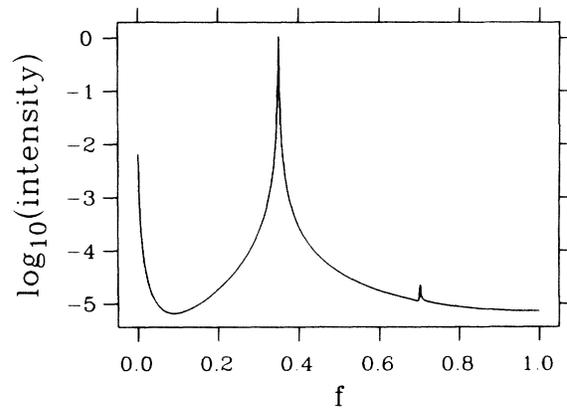

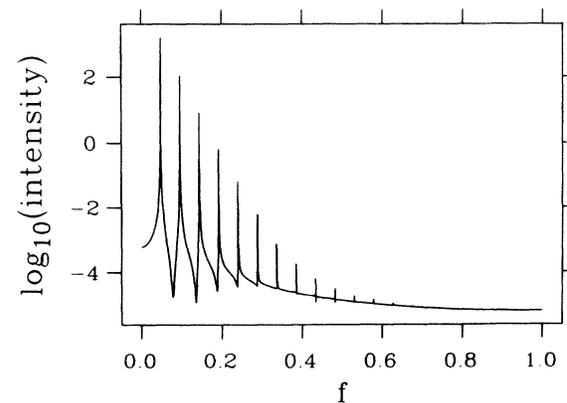FIG. 4. Power spectrum of a homogeneously oscillating state. Parameters: $l_T^{-1}=0.6$, $q=1.0$, and $v=1.0$.

FIG. 5. Power spectrum of a pure BP mode. Parameters: $l_T^{-1}=0.35$, $q=0.8$, and $v=1.0$.

harmonics—note the logarithmic intensity scale. All the spectra were obtained with a sufficiently large scanning frequency to avoid any appreciable aliasing [20].

Our dynamical system thus supports, in different regions of parameter space, three different types of oscillatory motion. These oscillators can interact nonlinearly, and it is interesting to note the dynamic consequences of this nonlinear coupling. For ease of discussion, we shall consider them pairwise; i.e., we focus on conditions where only two oscillators are important. In fact, we shall discuss only two of the possible pairings in order to identify a generic scenario. The third is the interaction between the VB mode and the homogeneous oscillator, which may lead to a different scenario, but which has not yet been investigated in detail.

For the sake of clarity, results will be presented in several complementary ways. To visualize the temporal evolution of the interface we use space-time portraits. A more detailed characterization of the dynamics will then be given in terms of power spectra and Poincaré maps.

B. First scenario

We begin by considering the interaction between VB and BP modes, within the symmetric model. For representations of these dynamic states, see Figs. 10 and 12 in I. The pure VB mode is symmetric about the central axes of the two oscillating cells, and exhibits spatial period doubling. As Fig. 2 demonstrates, pure VB and BP modes exist at very close locations in parameter space (the two squares at $l_T^{-1}=0.9$), i.e., they are expected to interact easily.

Let us now decrease l_T^{-1} at constant q, starting from the VB mode, i.e., we move along the path in parameter space indicated by the downward-pointing arrow in Fig. 2. The first event that we encounter is a *tertiary* instability; the pattern goes unstable with respect to parity breaking at $l_T^{-1} \approx 0.282$. Parity breaking results in a drift motion here as it did with stationary solutions. Figure 6 gives the space-time portrait corresponding to $l_T^{-1}=0.28$. Each point of the interface with a fixed lateral coordinate exhibits a superposition of two oscillatory motions: one stemming from the drift, with an associated frequency $f_1=qv$; the other from the persisting vacillating-breathing dynamics, with a different frequency f_2. We thus have two oscillators in a single spatiotemporal pattern. The corresponding two frequencies can be easily identified in the power spectrum of this state, displayed in Fig. 7, which is composed of combination frequencies of the form $|mf_1+nf_2|$, where m and n are integers.

Notice that such a spectrum might correspond to two different situations. Either the ratio of f_1 and f_2 is rational or it is not. In the first case, we would have periodic dynamics again (all frequencies could be considered harmonics of a common divisor of f_1 and f_2); in the second, the motion would be *quasiperiodic*. Which of the two cases is realized cannot easily be decided on the basis of a spectrum. This question is best analyzed in terms of *Poincaré maps*. Figure 8 gives the Poincaré map corresponding to the dynamics of Fig. 6.

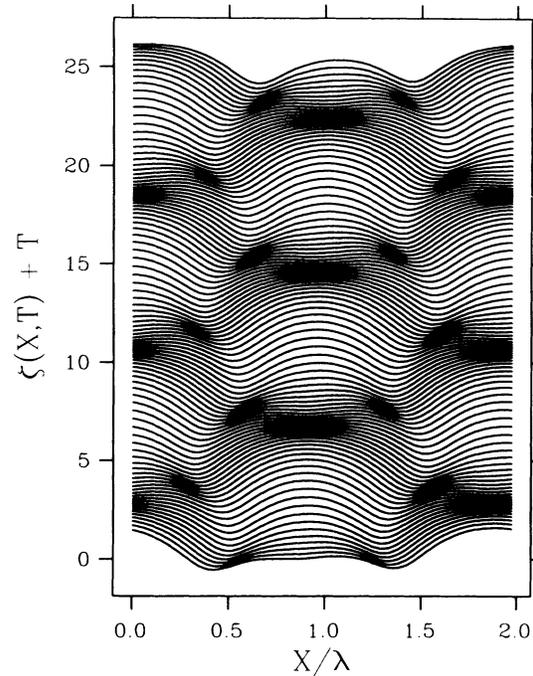This Poincaré map and all the others in this paper were

FIG. 6. Space-time portrait of quasiperiodic interface dynamics stemming from the superposition of drift and vacillating-breathing motions. The rules for these portraits are the same as in I, i.e., the y axis is a hybrid space-time coordinate, its units are the usual nondimensional ones; and the x axis is purely spatial, with units given by the wavelength of the basic symmetric solution, i.e., the largest x coordinate gives the aspect ratio. Parameters: $l_T^{-1}=0.28$, $q=0.9$, and $v=1.0$.

constructed as follows. Both amplitude ζ and velocity $\dot{\zeta}$ of a fixed point of the interface were measured during its temporal evolution. Each time the velocity crossed a predetermined value in a given direction, the amplitude was recorded. Considering the $(\tau+1)$st amplitude a function of the τth one, we obtain a so-called *one-sided* Poincaré map [21,22]. Now the Poincaré map of a periodic system clearly consists of a finite set of discrete points. In the simplest situation, the same velocity will be taken on only twice per oscillation, and only one of
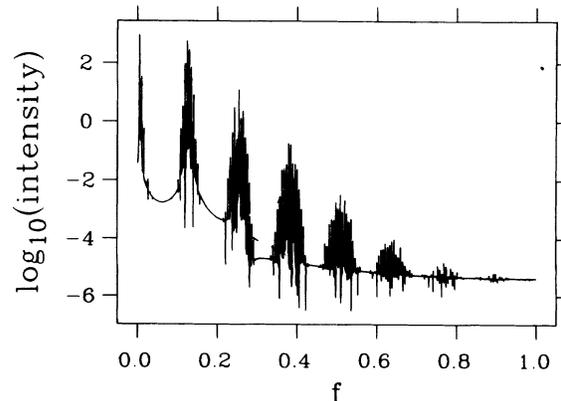

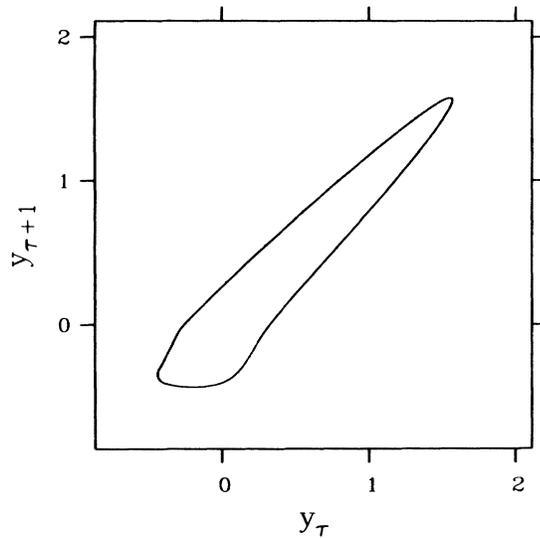FIG. 7. Power spectrum of the quasiperiodic state of Fig. 6.

FIG. 8. Poincaré map of the quasiperiodic state of Fig. 6.

FIG. 9. Poincaré map of a quasiperiodic state with temporal period doubling. Parameters: $l_T^{-1}=0.26$, $q=0.9$, and $v=1.0$.

these crossings will have the right direction (e.g., from smaller to larger velocity)—the Poincaré map then is just a single point. On the other hand, for quasiperiodic motion, no two intersections with the hypersurface will be at the same point, so the Poincaré map becomes an infinite set of points, which in two dimensions fill a (piecewise continuous) curve.

From the Poincaré map for the case $l_T^{-1}=0.28$ we infer that the tertiary instability has led to quasiperiodic motion, which means that the trajectories of the system densely cover a 2-torus in phase space. Of course, from a purely numerical analysis we can never be sure that we do not simply have a periodic orbit of very high periodicity. A physical argument against periodicity is that the two frequencies combining in the dynamics originate from two different oscillators that essentially have nothing to do with each other, namely the BP and VB modes. Thus there is *a priori* no reason for them to be related, and their ratio should be irrational with overwhelming probability. Only if *mode locking* occurs due to strongly nonlinear interaction of the two modes, will the dynamics become periodic again. Along the path $q=0.9$, l_T^{-1} decreasing, no mode locking was observed. However, mode locking does appear for different q values, as will be discussed below.

Let us continue our exploration of how the dynamics change when the control parameter l_T^{-1} is reduced. At first, the motion remains quasiperiodic, with increasing drift velocity.

At $l_T^{-1}=0.26$, the Poincaré map develops a second branch (Fig. 9), an event that is associated with *temporal period doubling*. A *subharmonic* of the lower frequency f_1 appears in the power spectrum, given in Fig. 10. This is the very first peak of the spectrum. That it represents a subharmonic rather than a basic frequency can be concluded from the fact that its intensity is almost two orders of magnitude smaller than that of the second peak. Due to this small intensity, the subharmonic is hardly
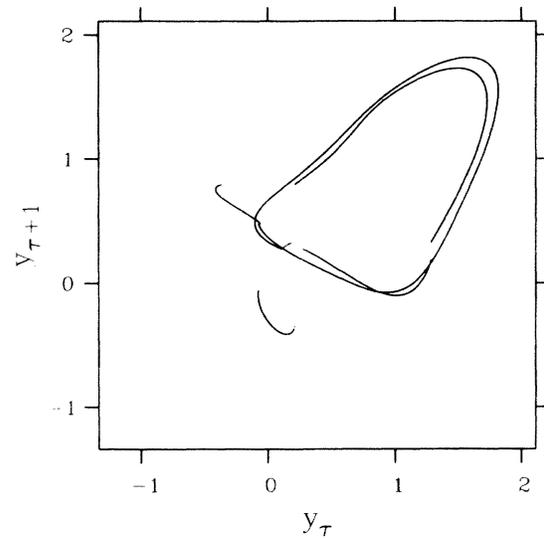
visible in the space-time portrait (Fig. 11). The only clue to its appearance is that the two laterally drifting cells are no longer identical.

The appearance of period doubling in time suggests the beginning of a subharmonic cascade toward chaos. However, we have not observed any further period doublings down to $l_T^{-1}=0.25$, where an additional low-frequency line appears (Fig. 12). Its frequency is 2.6×10^{-4}; the frequency associated with the drift is 2.0×10^{-2}, and its subharmonic is also present, which accounts for the first three peaks of the spectrum. Hence the new frequency is not related in any simple manner to the old ones. Figure 13 exhibits the Poincaré map of this dynamical state. It has dissolved into a cloud of points, which suggests the state to be chaotic. On the other hand, the spectrum still consists of well-separated lines, whereas for chaos we would expect a continuous background. Since the sampling time of both the Poincaré map and the spectrum was on the order of 10^4 [23], which corresponds to just a few oscillations at the lowest frequency of the spectrum, a
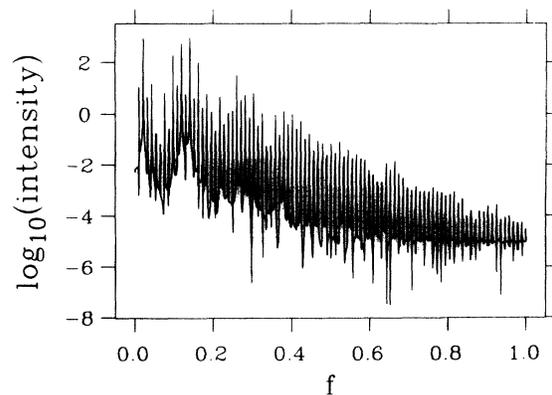

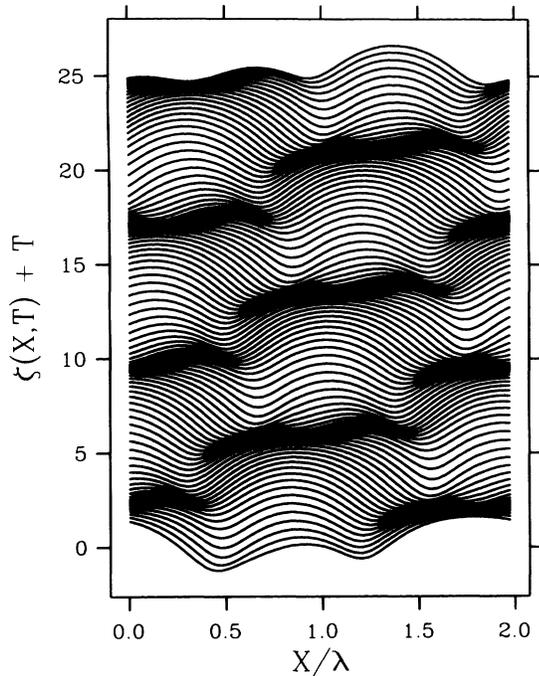FIG. 10. Power spectrum of the time-period-doubling state of Fig. 9.

FIG. 11. Space-time portrait of the time-period-doubling state of Figs. 9 and 10.

quasiperiodic state could also explain the general appearance of the Poincaré map. In Sec. IV we will reexamine this dynamic state by looking at its Lyapunov exponents.

In any case, the spectrum *does* acquire a background that is continuous within our resolution between $l_T^{-1}=0.25$ and 0.2495. The transition to chaos is located somewhere between $l_T^{-1}=0.251$ and 0.2495—we scanned the interval between $l_T^{-1}=0.255$ and 0.245 in steps of length 0.001 to bracket the transition point. A more detailed discussion of chaotic states will be given in Sec. IV.

As mentioned above, we did not see any sign of mode locking in following this path toward chaos. Table I gives measured values of the two basic frequencies appearing in quasiperiodic states and their ratios f_2/f_1. Of
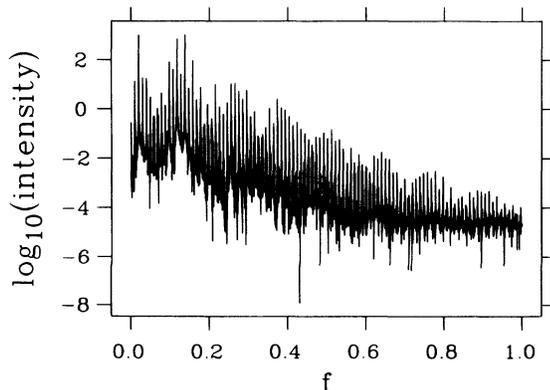

FIG. 12. Power spectrum of the state at $l_T^{-1}=0.25$, $q=0.9$, and $v=1.0$, after transients have decayed.
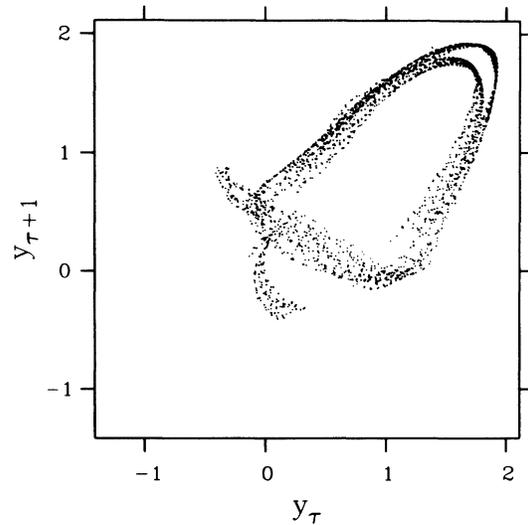

FIG. 13. Poincaré map of the state of Fig. 12.

course, we might simply have missed the exact value of a parameter where mode locking appears. But the fact that the overall shape of the attractor (or rather its cross section defined by the Poincaré map) remains unchanged lends some plausibility to the idea that mode locking is indeed avoided along this path.

To summarize, a quasiperiodic scenario toward chaos has been found in a realistic model for directional ordering of liquid crystals. Our suggestion is that this scenario is generic for systems that possess the drift instability and some other oscillatory mode [2].

1. One-sided model

We have verified that essentially the same scenario for a transition to chaos exists in the one-sided model, which is more appropriate for the description of conventional materials. In I, we showed by explicit examples that both the BP and VB modes are also present in the one-sided case (Figs. 12 and 13 there). An example for a quasiperiodic state is given in Fig. 14.

However, a systematic investigation of the dynamics as l_T^{-1} is lowered is quite cumbersome in the true one-sided model, because with increasing complexity of the motion the tendency of the interface to develop cusp singularities also increases. Once a cusp appears, it inevitably leads to failure of the dynamic integrator. For this reason, we have not been able to follow the dynamics of a *chaotic* state with $v=0$ for any reasonable amount of time. The

TABLE I. Dominant frequencies of dynamic states with $q=0.9$, $v=1.0$, and $k=1.0$.

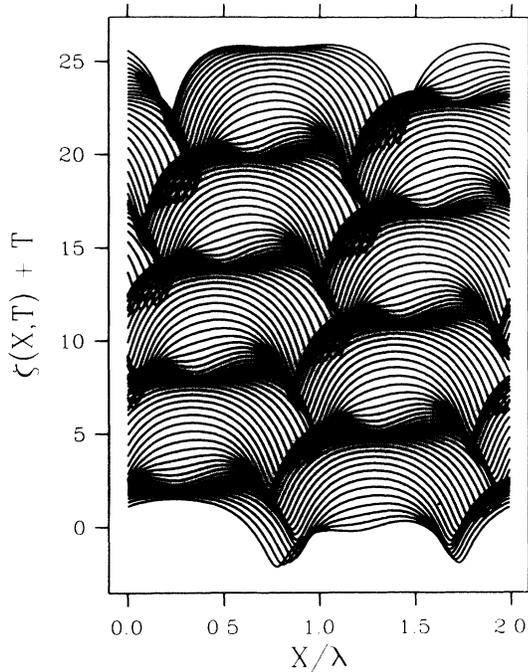| l_T^{-1}	f_1	f_2	f_2/f_1	Additional frequencies
0.28	5.4×10^{-3}	0.1244	23.14	
0.27	0.0201	0.1211	6.02	
0.26	0.0216	0.1198	5.54	$f_1'=0.0108$
0.25	0.0200	0.1179	5.89	$f_1'=0.0100$ $f_3=2.6\times10^{-4}$
0.24	0.0184	0.1158	6.30	many

FIG. 14. A quasiperiodic state of the one-sided model. Parameters: $l_T^{-1}=0.45$, $q=1.0$, and $v=0.0$.

state would always manage to produce a fluctuation that leads to a cusp.

Therefore, we chose v different from zero but small ($v=0.05$), to simulate an almost one-sided situation. We found the following sequence of dynamic states at constant wave number $q=1.1$: $l_T^{-1}=0.47$ is vacillating breathing; $l_T^{-1}=0.42\rightarrow0.38$ is quasiperiodic by superposition of VB and BP; and $l_T^{-1}=0.37$ and lower is chaotic.

2. "Order parameter"

In the theory of phase transitions or stationary bifurcations, it is customary to characterize the possible states by an order parameter. Because order parameters are defined via the properties of a state at a given time, they become time dependent for time-variable states.

However, it is possible to characterize globally our dynamic states by appropriate time-averaged quantities. Consider, for example, the spatially averaged interface position $\langle \zeta \rangle(T)=\langle \zeta(X,T) \rangle$. For *stationary* states, this is a constant, i.e., the standard deviation from its time average $\overline{\langle \zeta \rangle}$ is zero. (We denote averages over spatial fluctuations by angular brackets, and averages over temporal fluctuations by a bar.) On the other hand, this standard deviation will be positive for any persistent time-dependent state, provided the time dependence is different from a simple translation along the X axis. Therefore, we can introduce it as a characterizing parameter for the dynamics of any state:

$$\Delta_\zeta \equiv \overline{\langle \zeta(X,T) \rangle^2 - \overline{\langle \zeta(X,T) \rangle}^2}^{1/2} , \qquad (3.1)$$

where

$$\overline{A(T)} \equiv \lim_{T \to \infty} \frac{1}{T} A(T) . \qquad (3.2)$$

Since our states are pinned by the thermal gradient, we expect the averages $\overline{\langle \zeta \rangle}$ and Δ_ζ to exist for $l_T^{-1} \neq 0$.

Clearly, for nondrifting oscillatory states, Δ_ζ will increase with the amplitude of oscillation. Therefore, the bifurcation from a stationary state to an oscillatory state can be detected by monitoring Δ_ζ. Furthermore, it is also possible, as is demonstrated by Fig. 15, to see the bifurcation to a quasiperiodic state in the behavior of Δ_ζ as a function of l_T^{-1}. To accomplish this, we must be able to produce the VB mode beyond the bifurcation point, in order to compare its characterizing parameter with that for quasiperiodic motion. However, the drift motion can easily be suppressed by imposing, instead of periodic boundary conditions in a system with aspect two, reflecting boundary conditions in one with aspect ratio one. The two-cell structure then remains periodic at the doubled periodicity, but drifting states are impossible because the two symmetry axes pin the pattern. This procedure gives the inverted triangles in Fig. 15, while the triangles correspond to the dynamic states of the scenario discussed. With symmetry enforced, the VB mode survives down to $l_T^{-1}=0.245$, where the two cells start to become inequivalent. At $l_T^{-1}=0.24$, the temporal periodicity has tripled, and at $l_T^{-1}=0.235$ the spatiotemporal pattern begins to look chaotic.

We find that above $l_T^{-1}=0.28$, the dynamic states of both systems are identical. At $l_T^{-1}=0.303$, there is a bifurcation from stationary symmetric cells to the VB mode. Below $l_T^{-1}=0.28$, the drift motion first keeps Δ_ζ smaller in the quasiperiodic system than in the symmetric one (a pure drifting state has $\Delta_\zeta=0$). But as the dynamics become more complex in the nonsymmetric system, the characterizing parameter increases more quickly, and it soon exceeds that of a pure VB mode. Even the transi-
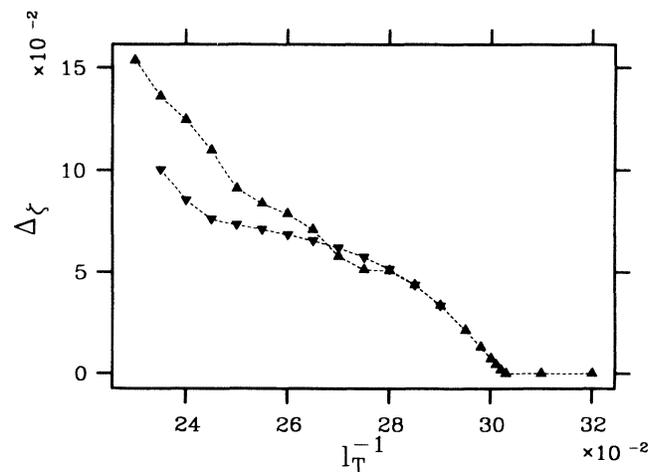

FIG. 15. The parameter Δ_ζ vs l_T^{-1} for periodic boundary conditions (triangles) and reflecting boundary conditions (inverted triangles), along the path given by the down arrow in Fig. 2. In the second case, the spatiotemporal pattern remains vacillating-breathing between $l_T^{-1}=0.303$ and $l_T^{-1}=0.245$. The dashed lines are drawn to guide the eye.

DIRECTIONAL SOLIDIFICATION AT HIGH SPEED. II. ...

tion to chaos may be inferred from the figure; it corresponds to an additional increase in the (absolute value of the) slope of the curve.

C. Second scenario

Let us now consider another pairing of oscillators in order to gather more evidence for the claimed genericity of a quasiperiodic scenario. The study to be described now was motivated by our earlier investigation of a two-mode approximation to the full system dynamics (for $v=1$ and $k=1$). Brief and extended descriptions of this approach have been given in Ref. [3] and in I. A transition to chaos via quasiperiodicity was observed within this two-mode picture. Since only the wave numbers q and $2q$ are then present, where q corresponds to the periodicity of the fundamental symmetric state, the VB mode evidently cannot be captured by such a description—it contains a component $\propto e^{iqX/2}$ owing to spatial period doubling. Therefore, the second oscillator that interacts with the BP mode to generate quasiperiodicity must be something different. From the general appearance of the dynamic states to be discussed below, it appears that this is the homogeneous oscillator.

The path in parameter space investigated in Ref. [3] and shown in Fig. 2 has a constant value $l_T^{-1}=0.28$, while q decreases starting around 0.8. This region of parameter space is much farther from the Eckhaus-unstable band, where we first detected the homogeneous oscillator, than from the domain where the VB instability is predominant. Thus the interaction with the latter should be stronger than that with the homogeneous oscillator. In the coupled amplitude equations for the two modes, however, the VB oscillator is absent, and as q is decreased the system moves closer to the neutral curve outside which a long-lived oscillatory planar solution exists [Eq. (2.12)]. Therefore, the homogeneous oscillator may be expected to become increasingly important. Taking the full dynamics into account would mean that all three oscillators interact in this region, which provides for augmented complexity. This may be interesting, yet in order to be able to compare with the amplitude equations we must somehow suppress the VB mode. To do so is easy: If we restrict the aspect ratio to one, by imposing periodic boundary conditions for a period $2\pi/q$, the VB mode cannot develop, and the interaction between the BP mode and the homogeneous oscillator can thus be considered separately.

Having discussed the constant-q scenario to chaos, we may be much briefer in describing now the constant-l_T^{-1} one. We find a pure BP state between $q=0.8$ and 0.76. Slightly below this point, we again obtain quasiperiodic dynamics. A space-time portrait of the interface motion at $q=0.753$ is given in Fig. 16. Instead of showing a Poincaré map, we demonstrate the quasiperiodic nature of the state by a stroboscopic projection of a system trajectory. It was constructed by recording the position and velocity of an interface point at constant time intervals. The example of Fig. 17 definitely conveys the impression of a 2-torus.

The transition to chaos occurs somewhere between $q=0.7454$ and 0.7453, which can be seen from the power
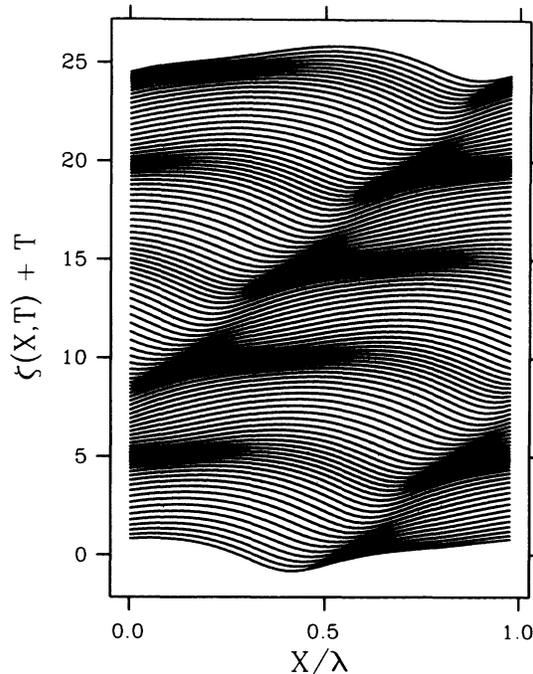

FIG. 16. Space-time portrait of quasiperiodic motion in scenario two. Parameters: $q=0.753$, $l_T^{-1}=0.28$, and $v=1.0$.

spectra and stroboscopic projections given in Figs. 18–21.

Contrary to the two-mode amplitude equations, the full model defined by Eq. (2.1) apparently does not exhibit mode-locking states along this path to chaos either. Most likely, they are destroyed by the influence of higher modes. The drastic change in the overall shape of the attractor during the transition to chaos (compare Figs. 20 and 21) may be a remnant of the mode-locking state that is present in the two-mode model. A similarly strong change of the attractor shape is not observed in the first scenario.
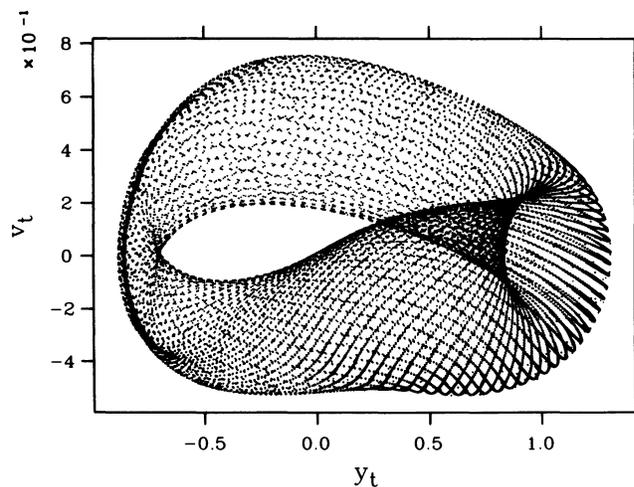

FIG. 17. Stroboscopic picture of a system trajectory for the quasiperiodic state of Fig. 16.
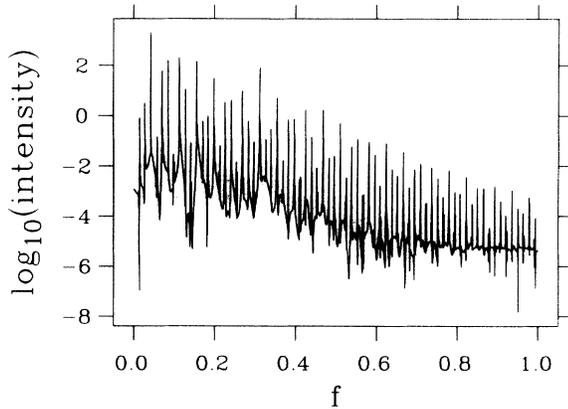
FIG. 18. Power spectrum for a quasiperiodic state close to the transition to chaos in scenario two. Parameters: $q = 0.7454$, $l_T^{-1} = 0.28$, and $v = 1.0$.
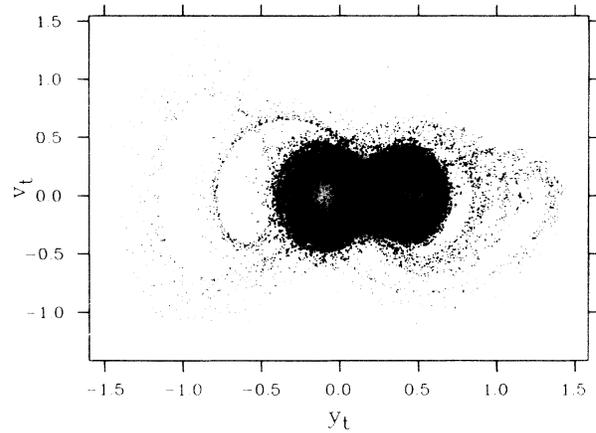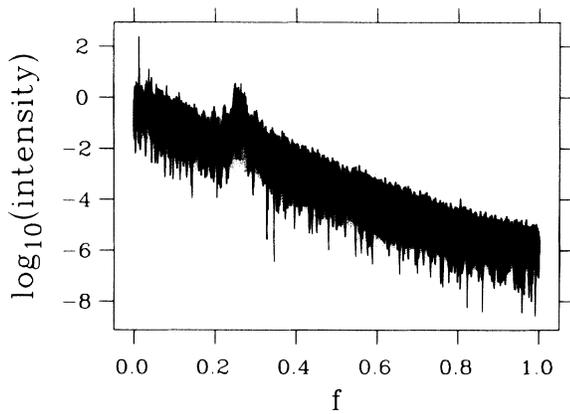

FIG. 19. Power spectrum for a state beyond the transition to chaos. Parameters: $q = 0.7453$, $l_T^{-1} = 0.28$, and $v = 1.0$.

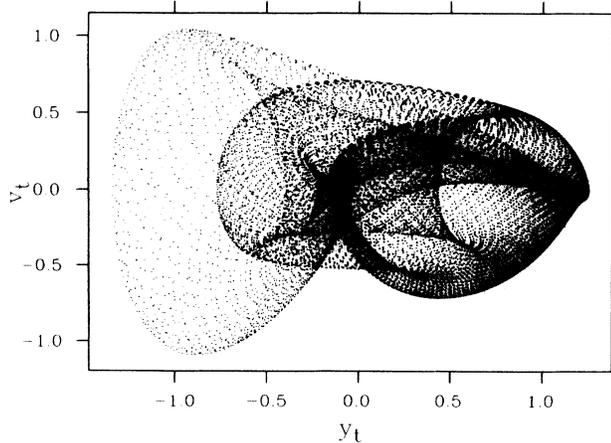FIG. 20. Stroboscopic map of the quasiperiodic state of Fig. 18.

FIG. 21. Stroboscopic map of the chaotic state of Fig. 19.

D. Mode locking and zigzag dynamics

Before closing this section, let us very briefly consider a case where mode locking *does* appear. Figure 22 shows the space-time portrait of a mode-locking state of order 5. Again, the Poincaré map (not shown) gives the relevant information in the most concise form—the state is periodic and the limit "cycle" makes five turns before it closes on itself. In the case presented, the fact of mode locking might also be guessed from the space-time portrait, which exhibits a long-time superstructure.

As the aspect ratio is increased, additional interesting dynamic states become possible, of which we show just a single example. Figure 23 presents the temporal evolution of an interface with $l_T^{-1} = 0.26$ and $q = 1.0$, and an aspect ratio of five. The interface starts moving left, changes direction after a while to drift to the right, changes direction again and continues this pattern by set-
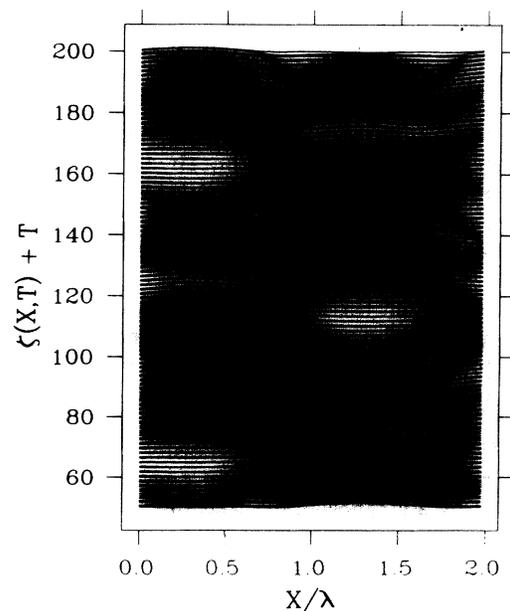

FIG. 22. Space-time portrait of a mode-locking state of order 5. Parameters: $l_T^{-1} = 0.256$, $q = 1.0$, and $v = 1.0$.
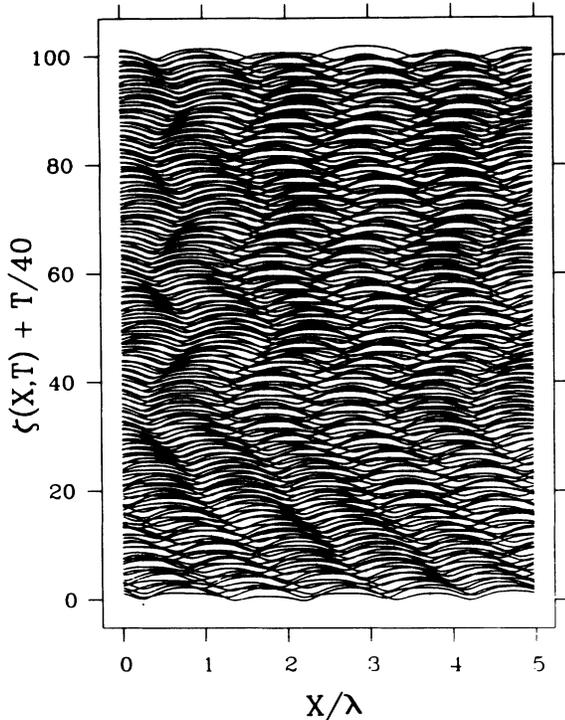
FIG. 23. Space-time portrait of transient zigzag dynamics. Here the time scale has been reduced by a factor of 40, to have several changes of the direction of motion in the picture. That is, the figure actually covers a time interval up to $T=4000$. Parameters: $l_T^{-1}=0.26$, $q=1.0$, and $v=1.0$.

tling into a zigzag motion. Apparently, this type of dynamics has already been observed in experiments. Here the zigzag motion is damped, but it persists up to $T=11\,000$ and beyond [23] (the period of the superimposed oscillation is 8.3), i.e., the damping is very weak.

Finally, it may be mentioned that a transition to chaos also takes place as l_T^{-1} is decreased starting from $q=1.0$ or a larger q value. For these parameters, the drift instability is very weak, and different scenarios, as yet hardly studied, are probable. This remark may serve to convey an impression of the richness of the dynamics inside the stability tongue, which should be a rewarding topic for further research.

IV. INSIDE THE CHAOTIC REGIME

A. General characterization of dynamics

The purpose of this section is to examine in more detail a few of the chaotic states that lie beyond the transition point. As an additional tool of characterization we will employ Lyapunov exponents. This will allow us to estimate the effective number of degrees of freedom needed to model the system by simpler equations. We shall see that this number is always larger than three for our system, and why this is so.

Formally, an interface that is described by a continuous coordinate has infinitely many degrees of freedom. However, in our small-aspect-ratio systems, spatial

coherence was always preserved, and chaos remained purely temporal. This means that the number of active degrees of freedom is finite, a fact which is the rationale behind any attempt to model the system by a small number of modes.

We first consider a point from the constant-q path of scenario one. Figures 24 and 25 represent the spectrum and Poincaré map of a state with $l_T^{-1}=0.24$. The spectrum is much noisier than that of Fig. 12 and clearly exhibits a continuous background of frequencies. From the Poincaré map, we infer that the 2-torus of the quasiperiodic motion has broken up. Its general outline is still present, but the trajectories fill its interior densely. We determined the fractal dimension of the point cloud in Fig. 25 by box counting, which yields a value of roughly $d_f=1.7$ (with an embedding dimension $d_e=2$). This result would suggest that the attractor has a fractal dimension of ≈ 2.7. However, examining larger embedding dimensions, we reconfirm the notorious impracticality of box-counting algorithms for calculating the dimension of strange attractors [24]. Therefore, at this point, we have a lower bound for the dimension of the attractor at best.

In Fig. 26, we give an example for the evolution of this system for a long enough time to make the irregular chaotic dynamics conspicuous.

If we continue to decrease l_T^{-1}, the motion first becomes more irregular. Eventually, its character changes dramatically. Figures 27 and 28 give the Poincaré map and spectrum of a system at $l_T^{-1}=0.22$. Because in this dynamics velocities are typically very small, we took $\dot{\zeta}=0$ as the threshold value, in order to be able to sample enough points. (In the previous Poincaré maps, the threshold value was 0.2, yielding maps very similar to those obtained for a value of 0.) The point density is now concentrated around a few points, and the spectrum shows an enhanced intensity near $f=0$, which is characteristic for intermittent chaos. This is indeed what we observe. The space-time portrait demonstrates that the interface is almost stationary for long periods of time, then bursts into irregular motion to end up in a state which is shifted by half a wavelength, corresponding to a jump of π in the phase of the pattern (Fig. 29).
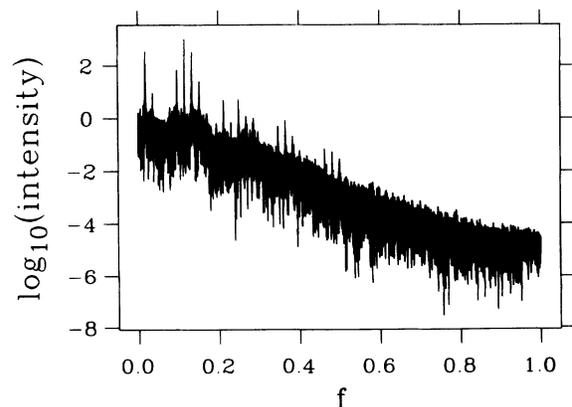

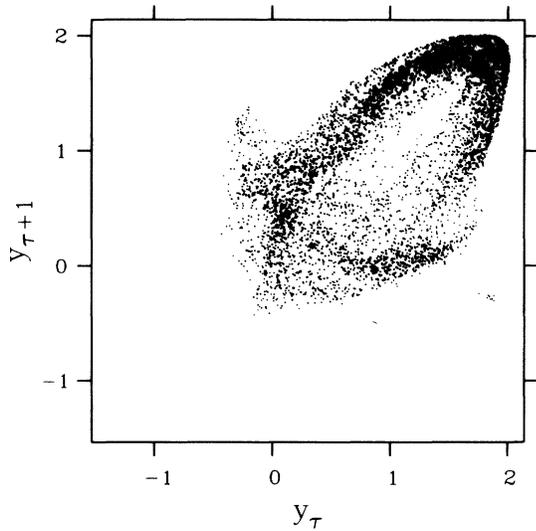FIG. 24. Power spectrum of a chaotic state in scenario one. Parameters: $l_T^{-1}=0.24$, $q=0.9$, and $v=1.0$.

FIG. 25. Poincaré map of the state of Fig. 24.

FIG. 27. Poincaré map of the state with $l_T^{-1}=0.22$, $q=0.9$, and $v=1.0$.

Along the path of the second scenario ($l_T^{-1}=0.28$), we find dynamic states that appear quite similar at first sight. The Poincaré map and the stroboscopic projection of the trajectory (Figs. 20 and 21) seem to collapse at the transition point, and the attractor immediately acquires a two-center structure. Somewhat deeper in the chaotic regime, at $q=0.73$, one finds an example where this structure is very prominent, as the stroboscopic picture of Fig. 30 exhibits. The motion of the system is easily characterized: while it sits on a spiral, we have more or less homogeneous damped oscillations, until the central turn of a spiral is reached. Then the amplitude of the interface changes rapidly, throwing the system on the other spiral from
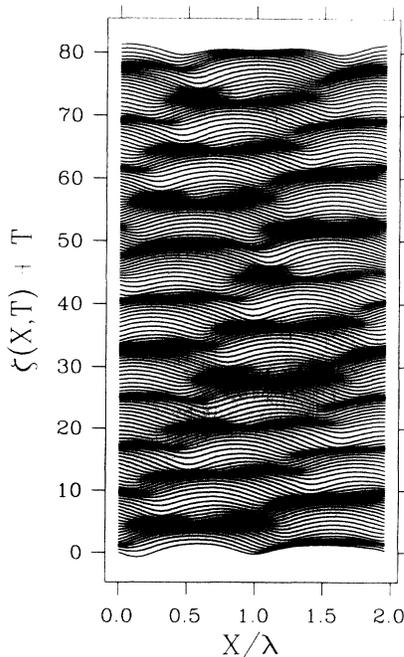
where it moves inward again. Figure 31 confirms this description directly. Note the main difference between the intermittent motion here and that in scenario one: there the quiescent state between two bursts was almost stationary, here it is oscillatory.

Inspection of Figs. 30 and 21 suggests that the state at $q=0.73$ is *less* chaotic than the one at $q=0.7453$. Clearly, such a possibility exists. We could have hit a window inside the chaotic regime where the dynamics become more regular again. Moreover, other than in scenario one, the chaotic domain must be bounded from below, since at $q=0.564$ the planar interface becomes stable again. Indeed, if we decrease q to 0.7, we find an attractor that is essentially the same double spiral as for $q=0.73$, but without any thickness—it is just a single line. The Poincaré map becomes a set of seven discrete points, i.e., the motion is periodic. Therefore, in order to find out just how chaotic the state $q=0.73$ is, we need some measure for chaos. Such a measure is provided by the Lyapunov exponents. So we turn now to the task of their computation.
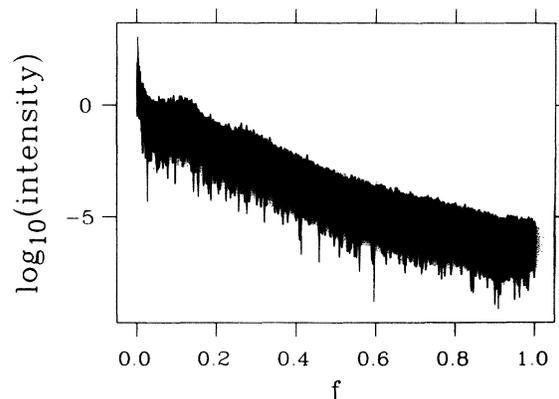

FIG. 26. Space-time portrait of the state of Fig. 24.

FIG. 28. Power spectrum of the state with $l_T^{-1}=0.22$, $q=0.9$, and $v=1.0$.
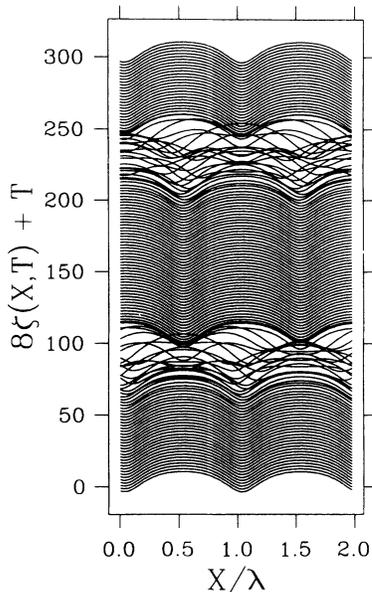
FIG. 29. Space-time portrait of the interface dynamics of the state of Fig. 27. Here the interface height has been multiplied by eight for better visibility.

B. Lyapunov exponents

Lyapunov exponents quantify the average rate of divergence or convergence of trajectories that are close to each other. Assume that we monitor the evolution of an infinitesimal n-sphere of initial conditions; then, due to the locally expanding or contracting nature of the flow, this sphere will turn into an n-ellipsoid. The ith Lyapunov exponent governs the growth rate of the ith principal axis $a_i(t)$ of the ellipsoid:

$$\lambda_i = \limsup_{t \to \infty} \frac{1}{t} \ln \frac{a_i(t)}{a_0(t)} , \tag{4.1}$$
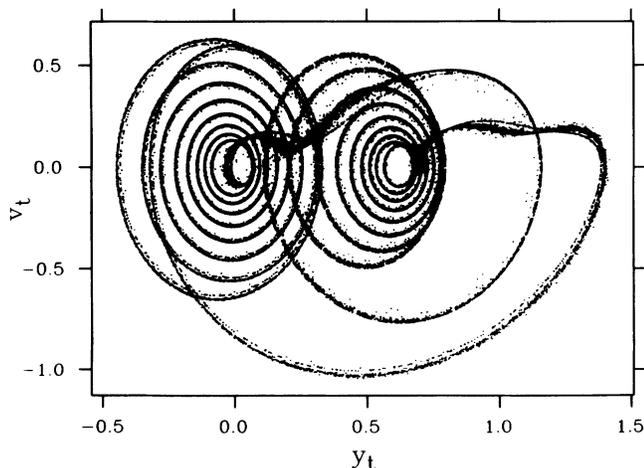

FIG. 30. Stroboscopic projection of system trajectory for a state lying beyond the transition to chaos in scenario two. Parameters: $q = 0.73$, $l_T^{-1} = 0.28$, and $v = 1.0$.
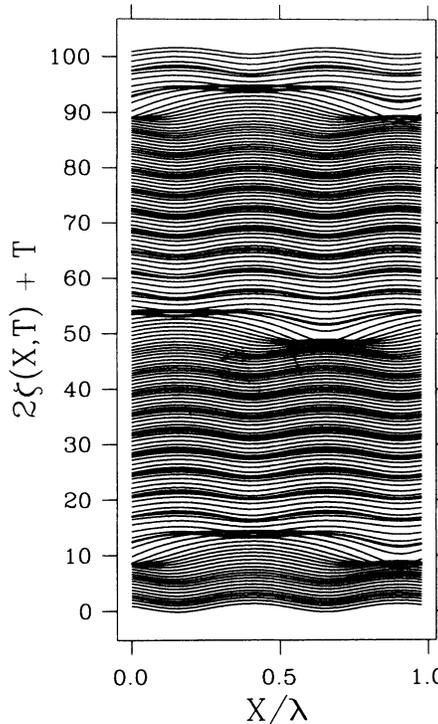

FIG. 31. Space-time portrait of the state of Fig. 30. The interface height has been multiplied by two for better visibility.

where $\lambda_1 > \lambda_2 > \cdots \lambda_n$ [25]. The "lim sup" stands here only to guarantee rigorously the existence of the exponent [26]; in many cases, the ordinary "lim" suffices. We can then say that the axis $a_i(t)$ grows as $e^{\lambda_i t}$ on average. Moreover, the sum of the first m Lyapunov exponents determines the growth rate of an infinitesimal m volume of phase space.

If we write the equations of motion of our dynamical system as

$$\dot{\mathbf{y}}(t) = \mathbf{M}(\mathbf{y}(t)) , \tag{4.2}$$

the Lyapunov exponents are calculable from the linear equation, also called the variational equation [21],

$$\dot{\mathbf{u}}(t) = L(\mathbf{y}(t))\mathbf{u}(t) , \tag{4.3}$$

where L is the linearization of $\mathbf{M}$ along the trajectory $\mathbf{y}(t)$. The Lyapunov exponent associated with a particular perturbation $\mathbf{u}(t)$ is given by

$$\lambda_u = \limsup_{t \to \infty} \frac{1}{t} \ln \|\mathbf{u}(t)\| , \tag{4.4}$$

where $\|\cdot\|$ is a suitably chosen norm (see Appendix B).

Almost all perturbations $\mathbf{u}$ will have a nonzero component in the direction of that solution to Eq. (4.3), whose norm grows fastest. Since this component will eventually dominate all others, one obtains the largest Lyapunov exponent λ_1 from almost all initial conditions by integrating Eq. (4.3). If, in an N-dimensional system, we require the initial condition to lie in the $(N-1)$-dimensional subspace that is orthogonal to the direction

growing as $e^{\lambda_1 t}$, almost all of these restricted initial states will yield, by the same argument, λ_2. Thus there is a sequence of nested perturbation subspaces $W_1 \supset W_2 \supset W_3 \supset \cdots W_N$ such that almost all perturbations in W_i evolve as $e^{\lambda_i t}$ on average [27].

For a system to be chaotic, at least one Lyapunov exponent must be positive. On the other hand, the sum of Lyapunov exponents of an attractor must be negative in a dissipative system, since contraction outweighs expansion.

A useful concept related to Lyapunov exponents is the *Lyapunov dimension,* introduced by Kaplan and Yorke

[28]. It is defined as

$$d_L = j + \frac{\lambda_1 + \lambda_2 + \cdots + \lambda_j}{|\lambda_{j+1}|} , \qquad (4.5)$$

where j is the largest integer for which $\sum_{i=1}^j \lambda_i \geq 0$. If all Lyapunov exponents are negative, d_L is set equal to 0. It has been conjectured [28] that d_L generically is equal to the *information* dimension of an attractor which in turn cannot exceed the *capacity* or fractal dimension d_f.

Let us now specify things for our system. Rewriting Eq. (2.1) as a system of first-order equations in time, and setting $u = \binom{u}{w}$, we obtain the variational equation

$$u_T = w ,$$

$$w_T = \left[2 + \frac{1}{k} + v \right] w_{XX} - \left[1 + \frac{1}{k} + v^2 \right] u_{XXXX} - 8ku_{XX} - 8kl_T^{-1}u + 2\zeta_{XX}w + 2\zeta_T u_{XX} + 4\zeta_{XT}u_X + 4\zeta_X w_X$$

$$- \left[4 + \frac{2}{k} + 2v \right] (2\zeta_{XX}u_{XX} + \zeta_{XXX}u_X + \zeta_X u_{XXX}) + 4v\zeta_{XX}u_{XX} - 12\zeta_X \zeta_{XX}u_X - 6\zeta_X^2 u_{XX} . \qquad (4.6)$$

In order to compute the set of the first m Lyapunov exponents, Eqs. (2.1) [in one dimension (1D)] and (4.6) must be integrated simultaneously. For the variational equation this must be done for m linearly independent initial con- ditions. Care has to be taken to avoid an alignment of the state vectors [given by $(u(X_1), \ldots, u(X_N)$, $u_T(X_1), \ldots, u_T(X_N))$, where the X_n are the discretization points] with the fastest-growing perturbation. How this can be achieved is explained in Appendix B.

Table II lists numerical estimates of the five or six largest Lyapunov exponents for various interesting dynamic states. The entry T_{av} refers to the finite-time interval used to approximate the infinite-time average in Eq. (4.4). Usually, after this time the last digit of the given exponents would be stable. An exception are the zero entries, where the achieved finite approximation of the exponent would normally fluctuate around zero (by its own order of magnitude). The numbers in brackets indicate the approximation obtained at the latest time for which the average was evaluated (i.e., at T_{av}). In some cases, the larger exponents were averaged over a longer time span than the smaller ones, which were already well converged.

A peculiarity to be noted is the abundance of cases with two vanishing Lyapunov exponents. In particular, for chaotic motion we always have two exponents that are zero, and the signature of the sequence of exponents is $+,0,0,-,-,\ldots$ or $+,+,0,0,-,\ldots$, corresponding to a *chaotic torus.*

We shall now present an argument why such a structure is bound to appear here. It is well known that in continuous-time systems at least *one* Lyapunov exponent vanishes for any bounded trajectory not ending in a fixed point [26]. The reason is simply that $\dot{y}$ solves the variational Eq. (4.3). Because this solution is bounded, we must have $\lambda_{\dot{y}} \leq 0$; on the other hand, if $\lambda_{\dot{y}}$ were negative, $\dot{y}$ would have to decay to zero as $t \to \infty$, and the system

would approach a fixed point, which was excluded by assumption.

Our system is not only continuous in time but also in space. Moreover, due to *translational invariance* the variational equation is solved by $y_X = (\zeta_X / \zeta_{XT})$. However, then we can mimic Haken's [26] argument for $\dot{y}$. Clearly, y_X is bounded (except possibly for $v = 0$). Furthermore, inside the stability tongue, it does not reduce to zero identically—otherwise the planar front solution of Eq. (2.12) would be stable. We conclude that there must be a second vanishing Lyapunov exponent whenever ζ_T and ζ_X are linearly independent. For a chaotic state, we believe this to be true generically.

As a consequence, the Lyapunov dimension of chaotic attractors must be strictly greater than three, and hence at least *four* real variables are necessary in any reconstruction of the system.

We may even extend this result to conjecture: If a dynamical system defined in d-dimensional position space is invariant under arbitrary continuous translations, and if it becomes chaotic, its strange attractor will generically have a fractal dimension that exceeds $d + 2$. Thus one- or two-dimensional interfaces and three-dimensional volumes would have attractors with dimensions larger than three, four, and five, respectively. This means that even if the number of degrees of freedom can be reduced to very few active modes, the difference between a truly zero-dimensional system (such as the Lorenz model) and one with larger dimension may be visible in the final complex dynamics. If the dimension of the attractor is between two and three, the reduced description cannot originate from an interface whose dynamics is translationally invariant. Of course, the conclusion cannot be reversed: If the fractal dimension of an attractor exceeds four, it need not belong to a two- or higher-dimensional system. Indeed, the dynamics of our interface do reach this level of complexity as can be seen from the entry for

$(q,l_T^{-1})=(0.9,0.24)$ in Table II.

Let us next turn to the VB mode $(l_T^{-1}=0.29)$. Here the Lyapunov dimension of the attractor is *two*, even though the motion is confined to a limit cycle. Again, this is a consequence of translational invariance. While a given set of initial conditions leads to a single limit cycle, a different set may lead to a final state which is dynamically equivalent but translated laterally. Hence globally the attractor is a tube—or torus, if the periodicity of boundary conditions is invoked—consisting of identical limit cycles, labeled, e.g., by the X coordinate of a symmetry axis of the VB mode. Of course, the attractor is *decomposable*, because any limit cycle itself is an attractor. The Poincaré map gives a single point—the global attractor does not show up in it. Since the calculation of Lyapunov exponents is based on considering perturbations, including small translations, the effect of the translational mode becomes visible.

Similarly, a stable *fixed point* $(l_T^{-1}=0.32)$, which normally has only negative Lyapunov exponents, is characterized by a Lyapunov dimension of one (instead of zero), because in reality the attractor is a line of states (with $\zeta_X\neq0$) that are images of each other under spatial translation.

For the drifting mode, we have $\zeta_X=-v\zeta_T$, i.e., the time derivative and the translational mode are linearly dependent. Thus there is only one vanishing exponent (see the entry for $q=0.8$, $l_T^{-1}=0.35$).

As the VB mode starts to drift, the Lyapunov dimension does not change, even though the Poincaré map changes drastically. What happens is that the attractor is no longer decomposable—the phase-space point of a single system now travels the whole attractor; there is no subset that is an attractor itself.

Finally, let us discuss the transition to chaos. If the Lyapunov exponents depend continuously on system parameters, one exponent must cross zero *at* the transition point. Hence there must be a state with *three* vanishing Lyapunov exponents, which corresponds to a 3-periodic state, i.e., a quasiperiodic state having three basic frequencies. For the state at $l_T^{-1}=0.25$, we find that its largest Lyapunov exponent is still decreasing after we have continued the averaging for the first Lyapunov exponent three times as long as for the others which were already converged. So we think that this might be a 3-periodic state, or a very slightly chaotic one.

TABLE II. Lyapunov exponents ($v=1.0$ and $k=1.0$).

(q,l_T^{-1})	(0.9,0.32)	(0.9,0.29)	(0.9,0.28)	(0.9,0.26)
λ_1	0 $[-4.8\times10^{-3}]$	0 $[-4\times10^{-5}]$	0 $[8\times10^{-4}]$	0 $[6\times10^{-5}]$
λ_2	-0.041	0 $[1.8\times10^{-4}]$	0 $[4\times10^{-4}]$	0 $[8\times10^{-5}]$
λ_3	-0.046	-0.081	-0.012	-0.049
λ_4	-0.143	-0.116	-0.146	-0.049
λ_5	-0.147	-0.153	-0.146	-0.189
λ_6	-0.300	-0.153	-0.209	-0.189
T_{av}	3000.0	8000.0	3000.0	5250.0
d_L	1	2	2	2
Type of motion	stationary	VB mode	quasiperiodic	quasiperiodic

(q,l_T^{-1})	(0.9,0.25)	(0.9,0.249)	(0.9,0.24)	
λ_1	0 $[4\times10^{-4}]$	$+0.045$	$+0.077$	
λ_2	0 $[-10^{-4}]$	0 $[8\times10^{-4}]$	0 $[3\times10^{-4}]$	
λ_3	0 $[6\times10^{-5}]$	0 $[2.6\times10^{-3}]$	0 $[10^{-5}]$	
λ_4	-0.007	-0.073	-0.054	
λ_5	-0.200	-0.211	-0.225	
λ_6	-0.201	-0.216	-0.237	
T_{av}	λ_1: 35 252.0 λ_2–λ_5: 11 252.0 λ_6: 10 252.0	3459.0	λ_1–λ_4: 9476.0 λ_5–λ_6: 7700.0	
d_L	3.0	3.6	4.1	
Type of motion	3-periodic (?)	chaotic	chaotic	

(q,l_T^{-1})	(1.0,0.6)	(0.8,0.35)	(0.7453,0.28)	(0.73,0.28)
λ_1	0 $[-3\times10^{-6}]$	0 $[-5.5\times10^{-3}]$	0.028	0.032
λ_2	-0.005	-0.058	0.015	0.008
λ_3	-0.005	-0.064	0 $[-2\times10^{-4}]$	0 $[5\times10^{-5}]$
λ_4	-0.107	-0.144	0 $[-2.7\times10^{-3}]$	0 $[-3.6\times10^{-3}]$
λ_5	-1.358	-0.149	-0.144	-0.250
λ_6		-0.175		
T_{av}	3162.0	3000.0	λ_1–λ_4: 33 406.0 λ_5: 30 076.0	λ_1–λ_4: 25 935.0 λ_5: 24 175.0
d_L	1	1	4.3	4.2
Type of motion	stationary	drifting	chaotic	chaotic

At $l_T^{-1} = 0.249$, we already have well-developed chaos with a Lyapunov dimension of 3.6, and at $l_T^{-1} = 0.24$ the Lyapunov dimension is 4.1.

While the Lyapunov exponents for the systems along the path of scenario one usually converged reasonably quickly, much longer averaging was necessary for the last two systems, taken from the path of scenario two. In the former cases, the sequence of magnitudes of the exponents remained unchanged (except for the two exponents that tend to zero), after short transients had decayed, and an increase of the number of discretization points did not influence the final values. For the latter two examples, the largest exponent did not separate well from the others when a coarse discretization (representing the interface by 45 points) was used; furthermore, the fourth exponent became the largest after some time, suggesting failure of the method (see Appendix B).

After increasing the discretization (to 81 points), the largest exponent separated early and persistently from the others, and the sequence of magnitudes of the exponents was as expected. In both systems, exponent No. 4 again started to increase around $T = 4600$, but this time it did not cross the value zero. Instead, at $T \approx 12\,000$ (for $q = 0.7453$) and $14\,000$ (for $q = 0.73$), exponent No. 2 started to increase. Thus the sequence of exponent magnitudes stayed in decreasing order. Although the exponents seem to be converged at the final times given, and further fine graining of the discretization (to 135 points) did not affect their values, it is clear that due to the possibility of even longer transients than those described (lasting $8000-10\,000$ time units) we cannot really claim these exponents to be accurate to the given three decimal places. For the patterns from scenario one or, more generally, farther inside the neutral stability curve, we did not observe transients of comparable length. Even for the two systems exhibiting these transients, the Lyapunov *dimension* turned out to be rather insensitive to the final fluctuations of the exponents, so its value should be more trustworthy.

In any case, our final estimates, given in the table, support the impression that chaos is already strong at $q = 0.7453$, and that the complexity of the corresponding attractor is higher than that of the system at $q = 0.73$ which has a smaller Lyapunov dimension, although its first Lyapunov exponent is larger. The difference in Lyapunov dimensions between the two systems is mostly determined by the different magnitudes of the fifth exponent.

V. SUMMARY

In this paper, we have described in some detail how the interaction of two oscillators, one of which corresponds to a drift motion, leads to quasiperiodic states, constituting the beginning of a scenario toward chaos. That this scenario possesses some genericity was demonstrated by two examples involving the interaction of different oscillators with the BP mode.

In the first case, we find that a vacillating-breathing oscillation is unstable with respect to parity breaking. The ensuing state consists of a superposition of the lateral drift and the VB oscillation. Because the ratio of the frequencies of the two basic modes is irrational, the dynamics are quasiperiodic, corresponding to motion on a 2-torus in phase space. As the control parameter is changed further, the system turns chaotic via a breakup of the torus. At the transition point, the Lyapunov dimension jumps from two to three. It increases fast in the chaotic domain and soon exceeds four. The final chaotic dynamics considered—a full characterization of the chaotic regime is not intended—show intermittent behavior, switching between nearly stationary states and chaotic intermezzos, leading to phase jumps.

We considered only small-aspect ratio systems here, so chaos was purely temporal and describable by a few degrees of freedom. Notwithstanding, the dimension of chaotic attractors is relatively high, a fact which we attribute to the translational invariance of the system.

The scenario described applies to the symmetric model as well as to a two-sided model with almost negligible diffusion in the solid phase.

Mode-locking states have been observed for q values that are relatively far from the line where parity-breaking states bifurcate, suggesting that they exist when the drift instability is not too strong.

In our second example for chaos via quasiperiodicity, the other oscillator besides the BP mode was a spatially homogeneous, i.e., purely temporal oscillation. The drifting state becomes unstable with respect to this oscillation as q is lowered. Characteristic of the subsequent dynamics is a drift motion of the interface which at the same time oscillates up and down as a whole. With increasing strength of the nonlinear interaction, the character of the motion changes to a periodic q-$2q$ hopping via tip splitting and recombination of (very flat) cells.

Again, a transition to chaos takes place. This time the invariant 2-torus seems to collapse completely within a very small parameter interval ($q \in [0.7453, 0.7454]$). It would be interesting to view this interval on a logarithmic scale. There is still room for a period-doubling cascade in this scenario, whereas in the first we believe that it is excluded by the appearance of a third frequency (which is not a subharmonic).

Once more, the chaotic state has an intermittent character, but now the states that alternate are an oscillation and a period of fast irregular motion leading to an effective phase jump. Furthermore, in the second scenario we know that the chaotic region is bounded from below.

Experimentally, it will be difficult to see these scenarios, since they require small aspect ratios. From simulations with larger aspect ratios it appears that the VB mode is stable, whereas the BP state is known to be long-wavelength unstable. Preliminary investigations suggest that depending on the value of l_T^{-1} it decays into a stable symmetric steady state, the VB mode, or a weakly turbulent state. There is also the possibility of a small band where quasiperiodic features survive (see I).

An interesting question with regard to spatiotemporal chaos for a very large aspect ratio is whether the deterministic equation of motion (2.1) leads to long-time and large-scale behaviors that can be described by a simpler stochastic equation. We have suggested that this equa-

tion cannot be the simplest possible nonlinear model for interface motion, which is the Kardar-Parisi-Zhang equation [13] (whose scaling properties agree well with those of the Kuramoto-Sivashinsky equation). We hope to deal with spatiotemporal chaos in more detail in the future

ACKNOWLEDGMENTS

APPENDIX A: NUMERICAL SOLUTION OF THE DYNAMIC EQUATION

1. Stationary solutions

In the one-dimensional case, our basic equation is a partial differential equation (PDE) for the two variables X and T:

$$\zeta_{TT} - \left[2 + \frac{1}{k} + \nu\right]\zeta_{XXT} + \left[1 + \frac{1}{k} + \nu^2\right]\zeta_{XXXX} + 8k\zeta_{XX} + 8kl_T^{-1}\zeta$$

$$= 2\zeta_T\zeta_{XX} + 4\zeta_X\zeta_{XT} - \left[4 + \frac{2}{k}\right]\zeta_{XX}^2 - \left[4 + \frac{2}{k} + 2\nu\right]\zeta_X\zeta_{XXX} - 6\zeta_X^2\zeta_{XX} \ . \quad \text{(A1)}$$

It is natural to look for stationary solutions to this first, because then the time derivative can either be dropped (for "true" stationary solutions) or replaced by a spatial derivative $\partial_T \to -\nu\partial_X$ (for solutions that are stationary in a frame moving laterally at velocity ν). Since the former situation is just a special case of the latter (corresponding to $\nu = 0$), we can condense both into a single equation:

$$\nu^2\zeta_{XX} + \nu\left[2 + \frac{1}{k} + \nu\right]\zeta_{XXX} + \left[1 + \frac{1}{k} + \nu^2\right]\zeta_{XXXX} + 8k\zeta_{XX} + 8kl_T^{-1}\zeta$$

$$= -6\nu\zeta_X\zeta_{XX} - \left[4 + \frac{2}{k}\right]\zeta_{XX}^2 - \left[4 + \frac{2}{k} + 2\nu\right]\zeta_X\zeta_{XXX} - 6\zeta_X^2\zeta_{XX} \ . \quad \text{(A2)}$$

The PDE has turned into an ordinary differential equation (ODE) which can be solved more easily and by other approaches than the fully time-dependent problem. Because Eq. (A2) is fourth order in space, its general solution depends on four constants of integration that may be prescribed in various ways.

In order to discuss this in more detail, let us, as is done in the numerics, rewrite the equation as a set of first-order equations:

$$\mathbf{y}'(X) = \mathbf{f}(\mathbf{y}(X)) \ , \quad \text{(A3)}$$

where $\mathbf{y}$ is a vector whose four components are $y_1 = \zeta$, $y_2 = \zeta_X$, $y_3 = \zeta_{XX}$, and $y_4 = \zeta_{XXX}$. $\mathbf{f}$ is not explicitly X dependent because of translational invariance.

If we seek solutions on the interval $[a,b]$, we can write the general integral of (A3) as

$$\mathbf{y}(X) = \mathbf{y}^{(0)} + \int_a^X dX' \mathbf{f}(\mathbf{y}(X')) = \mathbf{y}^{(0)} + \mathbf{F}(\mathbf{y}(X), \mathbf{y}^{(0)}) \ , \quad \text{(A4)}$$

where

$$\mathbf{y}^{(0)} = \mathbf{y}(a) \ . \quad \text{(A5)}$$

We have emphasized the dependence of the function $\mathbf{F}$ on the initial condition by writing $\mathbf{y}^{(0)}$ as an explicit argument.

To obtain symmetric solutions, we set the interval to half a wavelength and require the boundary conditions $\zeta_X(a) = \zeta_X(b) = 0$, and $\zeta_{XXX}(a) = \zeta_{XXX}(b) = 0$. This immediately fixes $y_2^{(0)}$ and $y_4^{(0)}$ and gives the two equations

$$0 = y_2(b) = F_2(\mathbf{y}(b), \mathbf{y}^{(0)}) + y_2^{(0)} \ ,$$
$$0 = y_4(b) = F_4(\mathbf{y}(b), \mathbf{y}^{(0)}) + y_4^{(0)} \quad \text{(A6)}$$

determining the two remaining components of $\mathbf{y}^{(0)}$.

In the general stationary case, we would like to impose periodic boundary conditions for an interval corresponding to a full wavelength, which implies

$$\mathbf{F}(\mathbf{y}(b), \mathbf{y}^{(0)}) = \mathbf{F}(\mathbf{y}^{(0)}, \mathbf{y}^{(0)}) = 0 \ . \quad \text{(A7)}$$

This is a system of four equations, which are, however, degenerate, if they are solvable at all. Indeed, if Eq. (A7) is solved by some nontrivial function $\mathbf{y}(X)$, it is also solved by $\mathbf{y}(X - X_0)$, with an arbitrary shift X_0, due to translational invariance. This means that $\mathbf{y}^{(0)}$ is not uniquely determined. Hence we can impose an additional condition on the solution to fix X_0. A failsafe way is to require $\zeta_X(a) = 0$, because any bounded solution must have extrema (while we cannot be sure than any prescribed nonzero value for ζ_X is taken on by the solution). But then the solution should depend on some additional parameter to compensate for this additional degree of freedom. This parameter is, of course, the drift velocity ν. Formally,

$$y_2^{(0)} = 0, \quad \mathbf{F}(\nu, \mathbf{y}^{(0)}, \mathbf{y}^{(0)}) = 0 \ . \quad \text{(A8)}$$

For a given value of v, either the second of these equations is not solvable or it is solvable for a one-parameter family of vectors $\mathbf{y}^{(0)}$. One of these solutions is then selected by the first equation. The velocity v itself is selected by the *condition of solvability*, which means that only a *discrete spectrum* of v values should exist, usually including $v=0$. So we can find both symmetric and asymmetric solutions by solving Eq. (A8), and the velocity is obtained as part of the solution.

In practice, the method is a combination of a shooting and matching technique with Newton's method for the solution of Eqs. (A6) and (A8). The word shooting is a fancy way to refer to the numerical construction of the function $\mathbf{F}$, which is done by integrating Eq. (A3) using some ODE solver, e.g., a Runge-Kutta method with automatic step size adaption. Since at the beginning we do not know the entire vector $\mathbf{y}^{(0)}$, we start from an initial guess of its missing components, and "shoot" to the other side of the interval with the ODE solver. This shooting has to be repeated iteratively until the boundary conditions there are satisfied too. In our second case, the parameter v is allowed to vary during the iteration process.

To obtain the iteration scheme, first write the nonlinear equations in the form

$$\mathbf{G}(\bar{\mathbf{y}}) = 0 , \qquad (A9)$$

where $\bar{\mathbf{y}} = (y_1^{(0)}, y_3^{(0)}, y_1(b), y_3(b))$ for Eq. (A6), and $\bar{\mathbf{y}} = (y_1^{(0)}, y_3^{(0)}, y_4^{(0)}, v)$ for Eq. (A8). Then by expanding $\mathbf{G}(\bar{\mathbf{y}}_i^n + \delta\bar{\mathbf{y}}_i) = 0$ to first order in the deviation $\delta\bar{\mathbf{y}}_i$ of the true solution from the nth approximant $\bar{\mathbf{y}}_i^n$, solving for $\delta\bar{\mathbf{y}}_i$, and setting $\delta\bar{\mathbf{y}}_i = \bar{\mathbf{y}}_i^{n+1} - \bar{\mathbf{y}}_i^n$, we arrive at

$$\bar{y}_i^{n+1} = \bar{y}_i^n - \left[\frac{\partial G}{\partial \bar{y}} \right]_{ij}^{-1} G_j(\bar{\mathbf{y}}) . \qquad (A10)$$

This is Newton's method for the multidimensional case, requiring the calculation of the Jacobian of $\mathbf{G}$, which is usually done by a finite differencing scheme.

There are refinements of implementation, but this is the principle of the method. We used the routines D02HAF and D02HBF from the Numerical Algorithms Group (NAG) FORTRAN library (Mark 14).

2. Dynamical evolution

To treat the full dynamic problem, we convert the PDE to an approximating set of $2N$ ordinary differential equations by setting $\mathbf{y}(T) = [\zeta(X_1, T), \zeta(X_2, T), \ldots, \zeta(X_N, T), \zeta_T(X_1, T), \ldots, \zeta_T(X_N, T)]$, where the X_n's are the discretization points: $X_n = (n-1)h$, $h = \Lambda/N$, and Λ is the imposed periodicity length. The equation of motion then takes the form (4.2), where the vector function $\mathbf{M}$ is determined by the discrete approximations, in terms of ζ, chosen for the derivatives ζ_X through ζ_{XXXX}. We employed both a direct discretization by molecules of second-order accuracy in h, and a spectral method. All results presented in this paper were obtained by the latter which, for the same grid spacing h, is slower than the direct method but much more accurate. In the calculation of Lyapunov exponents, this turned out to be particularly important.

Here is how the derivatives are computed. The vector $\mathbf{y}$ consists of two sets of N elements, $\mathbf{y} = (\mathbf{y}_1, \mathbf{y}_2)$, each of which represents a periodic function, namely ζ and ζ_T. Let us, for simplicity, consider just $\mathbf{y}_1$. First, we take its discrete Fourier transform

$$Y_{1k} = \sum_{n=1}^{N} y_{1n} e^{2\pi i k(n-1)/N} = \sum_{n=1}^{N} y_{1n} e^{iq(n-1)\Lambda/N} , \qquad (A11)$$

where k is an integer $(k = 0, 1, \ldots, N-1)$ and $q = 2\pi k/\Lambda$ is the wave number of Fourier component Y_{1k}. Then, we multiply Y_{1k} by iq, $(iq)^2$, and so on, to obtain the Fourier transform of the first, second, and so on, derivatives. Finally, we apply an inverse Fourier transform to obtain the derivatives themselves. This procedure is accurate to order h^N, i.e., it becomes an "infinite-order" method as N is increased.

Some limitations on the value of N follow from using this method. First, in order to make sure that the inverse transform of $(iq)^m Y_{1k}$ is real for odd m, N must be odd. Second, since we used an algorithm for fast-Fourier transforms, N had better consist only of small prime factors. Ordinarily, we took 45 or 81 discretization points for systems with aspect ratio one; 45, 81, 135, or 225 points for systems with aspect ratio two (the finer discretizations were needed in the one-sided model); and 225 or 345 points for larger systems. The discretization was varied to check the independence of the results. For systems with aspect ratios that are much larger than ten, the spectral method becomes impractical, because it does not allow to take advantage of sparse-matrix techniques.

Once the derivatives are known, we are in a position to integrate the dynamical equations forward in time. Since they are expected to be *stiff* (i.e., more than one time scale is present), an implicit integration method is used. For a discussion of stiffness, see Ref. [20].

The simplest and most instructive example for the difference between explicit and implicit methods is provided by the differential equation for the exponential function $[z(t) = ae^{-\mu t}]$:

$$\dot{z} = -\mu z . \qquad (A12)$$

Discretizing time according to $t = n\Delta t$, the lowest-order explicit differencing scheme would be

$$\frac{z_{n+1} - z_n}{\Delta t} = -\mu z_n \Longrightarrow z_{n+1} = (1 - \mu\Delta t)z_n , \qquad (A13)$$

while the simplest implicit scheme is

$$\frac{z_n - z_{n-1}}{\Delta t} = -\mu z_n \Longrightarrow z_n = \frac{z_{n-1}}{1 + \mu\Delta t} , \qquad (A14)$$

i.e., the forward difference for the time derivative has been replaced by a backward difference. In the explicit case, the new value of $z(z_{n+1})$ is explicitly given in terms of the old one (z_n), whereas in the implicit case an equation must be solved to express the new value (z_n) in terms of the old one (z_{n-1}).

For positive μ, the explicit method will obviously give an even *qualitatively wrong* behavior, if Δt is chosen too large $(\Delta t > 2/\mu)$, while the implicit method will converge to the correct stationary solution zero for any positive Δt.

Note that this is not a statement about accuracy but about stability. Accuracy always imposes restrictions on the allowable step size. On the other hand, for *negative* μ, the explicit method will always *correctly* exhibit unstable behavior, whereas the implicit one *wrongly* converges to zero for $\Delta t > 2/|\mu|$.

Thus, if the dynamics of a continuous system are stable, an explicit discretization may behave unstably, whereas for a chaotic continuous system implicit discretization may lead to stabilization, i.e., nonchaotic behavior. Therefore, if we find chaos with an *implicit* method, we can be reasonably sure that there is chaos.

When Eq. (A12) is generalized to a system of equations, the implicit method necessitates inversion of a matrix. With a nonlinear system, a fully implicit scheme would require the (iterative) solution of the nonlinear system of equations for the new values of the solution function at each time step. Therefore, usually the nonlinear operator is linearized about the function values of the last time step, i.e., the simplest temporal discretization scheme of Eq. (4.2) would then be

$$\frac{y^{(n+1)}-y^{(n)}}{\Delta t}=M(y^{(n)})+\left[\frac{\partial M}{\partial y}\right](y^{(n+1)}-y^{(n)}) \ ,$$

(A15)

where $(\partial M/\partial y)$ $[=L(y)]$ is the Jacobian M, evaluated at the old values $y^{(n)}$. Equation (A15) can be easily solved for $y^{(n+1)}$.

To specialize to our system, we implemented one of Gear's backward difference methods [18], using the routine DIVPAG from the International Mathematical and Statistical Library (IMSL), Houston. A fifth-order multistep algorithm was chosen, based on the formula

$$y^{(n+1)}=\tfrac{1}{137}\{300y^{(n)}-300y^{(n-1)}+200y^{(n-2)}-75y^{(n-3)}$$
$$+12y^{(n-4)}+60hM(y^{(n+1)})\} \ ,$$

(A16)

and a chord method was used, with a finite-difference evaluation of the Jacobian.

We also tried out an explicit Adams-Moulton method, but found that it was considerably slower than the Gear method, presumably due to excessive reduction of the step size in attempting to accurately integrate the stiff system.

APPENDIX B: NUMERICAL CALCULATION OF LYAPUNOV EXPONENTS

A direct computation of Lyapunov exponents from their definition is not normally feasible, for two reasons. In chaotic systems, there is at least one positive Lyapunov exponent, leading to exponentially growing solutions of the variational equation and the associated numerical problems. Furthermore, because of the tendency of almost all solutions to align with the fastest-growing one, it is difficult to find initial conditions that yield exponents other than λ_1.

The first of these problems can be solved by performing the integration of the variational equation in stages, normalizing the solution after each step, and adding up the logarithms of the growth factors. We are allowed to do

this because the variational equation is linear, so the normalized solution evolves exactly the same way as the unnormalized one. To master the second problem, we consider a set of orthonormal initial perturbations that are reorthonormalized after some time to keep them in different perturbation subspaces.

Here is the general scheme. We choose an initial condition for the dynamic equation (4.2) which determines the trajectory whose Lyapunov exponents we compute. These exponents are the same for all trajectories on the same attractor [21]. Furthermore, to compute m Lyapunov exponents we choose a set of orthonormal initial states u_i, $i=1,\ldots,m$, for the variational equation (4.3).

Then we evolve the perturbations according to the variational equation for some small enough time interval Δt so that the tendency of the vectors to line up does not yet render the calculation of their spanned volume inaccurate.

Next we orthonormalize the vectors $u(t)$ according to the Gram-Schmidt procedure, which can be condensed into the following recursion formulas $(i=1,\ldots,m)$:

$$v_i=u_i^{old}-\sum_{k=1}^{i-1}\langle u_i^{old},u_k^{new}\rangle u_k^{new} \ ,$$

(B1)

$$u_i^{new}=v_i/\|v_i\| \ ,$$

(B2)

where the sum is set equal to zero for $i=1$. The angular-bracket expression $\langle \cdot,\cdot \rangle$ denotes a scalar product in the Hilbert space associated with the phase space of the system, and $\|\cdot\|$ is the norm induced by this scalar product. The new vectors u_i span the same subspace as the old ones. An important point to note here is that the product of the norms of the auxiliary vectors v_i for $i=1,\ldots,l$ gives the volume of the parallelepiped in the l dimensional subspace spanned by the original vectors $u_1^{old},\ldots,u_l^{old}$. In fact, since the initial volume was 1, this is the *growth factor* of the volume during the considered time interval. Now we know that the sum of the first l Lyapunov exponents gives the average logarithmic growth rate for this l-dimensional volume. Hence we obtain an approximation to this sum by repeating the above sequence of evolution of the variational equation and subsequent orthonormalization K times, with K large enough, and by adding the logarithms of the growth factors $\prod_{i=1}^{l}\|v_i\|$, finally dividing by the total time to obtain the average:

$$\lambda_1+\lambda_2+\cdots+\lambda_l\approx\lim\frac{1}{K\Delta t}\sum_{k=1}^{K}\ln\prod_{i=1}^{l}\|v_i^{(k)}\|$$

$$=\lim\frac{1}{K\Delta t}\sum_{k=1}^{K}\sum_{i=1}^{l}\ln\|v_i^{(k)}\| \ ,$$

(B3)

where the superscript k refers to the time step after which the norm is evaluated. Specializing to $l=1$, we see that λ_1 is given by

$$\lambda_1\approx\lim\frac{1}{K\Delta t}\sum_{k=1}^{K}\ln\|v_1^{(k)}\| \ .$$

(B4)

Subtracting this from Eq. (B3) for $l=2$, we obtain

$$\lambda_2 \approx \lim \frac{1}{K\Delta t} \sum_{k=1}^{K} \ln\|\mathbf{v}_2^{(k)}\| , \tag{B5}$$

and, by induction,

$$\lambda_i \approx \lim \frac{1}{K\Delta t} \sum_{k=1}^{K} \ln\|\mathbf{v}_i^{(k)}\| . \tag{B6}$$

It should be mentioned that the members of the sequence λ_1, λ_2, etc., are not equivalent. λ_1 is computed from a perturbation that evolves freely apart from normalization; it is never forced to change its direction by orthogonalization. The perturbation corresponding to λ_2 is forced to be orthogonal only to that associated with λ_1; the next one has to be orthogonal to two predecessors, and so on. Thus the sequence of Lyapunov exponents obtained from the algorithm should be in descending order, except possibly for almost degenerate exponents.

In order to integrate the variational equation (4.3), one must simultaneously integrate the dynamic equation (4.2), because the former depends on $\mathbf{y}(t)$. Schemes suggested in the literature [21] often assume that for a given dynamical system all Lyapunov exponents are to be computed, which would mean that for our coarsest interface discretization, consisting of 45 points, corresponding also to 45 Lyapunov exponents, we would have to solve a system of $46\times45=2070$ equations. Of course, the time evolution matrix has a block structure, it consists of 46 blocks of 45×45 matrices (one for the dynamic equation, 45 for the variational equation). Therefore, the problem can be split up into 46 subproblems. However, most of these will yield negative Lyapunov exponents with large absolute values, in which we are not interested—especially since their number can be increased arbitrarily by refining the discretization. Therefore, we evolved only the dynamic equation together with the variational equation for a single Lyapunov exponent up to the end of the chosen basic time interval Δt; then we went back to the beginning of the interval to integrate the variational

equation for the second Lyapunov exponent, which meant integrating the dynamic equation a second time starting from its stored state at the beginning of the interval. This procedure was repeated for up to six exponents. It implies a certain overhead due to the repeated integration of the dynamic equation on the same time interval. Attempts to just integrate it once and interpolate the solution at intermediate times turned out to be insufficient in terms of accuracy. In any case, although definitely somewhat unsatisfactory with respect to elegance and efficiency, the method outlined is easy to program, and allows us to use a black-box integrator without having to worry about the instability problems sometimes encountered with sparse-matrix solvers. We employed the NAG routine D02EAF which uses a variable-order variable-step method implementing backward differentiation formulas.

Finally, the scalar product used in the numerics has to be specified. For the underlying continuous system we simply have

$$\left\langle \begin{bmatrix} f(X,T) \\ f_T(X,T) \end{bmatrix}, \begin{bmatrix} g(X,T) \\ g_T(X,T) \end{bmatrix} \right\rangle$$
$$= \int_0^\Lambda dX[f(X,T)g(X,T)+f_T(X,T)g_T(X,T)] . \tag{B7}$$

Since we evolve the dynamic equation with spectral accuracy, it is desirable to discretize the scalar product with high accuracy as well. Surprisingly, this can be achieved by using the simple trapezoidal rule, which due to the periodicity $(f_1=f_{N+1})$ of all pertinent functions reads

$$\int_0^\Lambda dX\, f(X)=h \sum_{i=1}^{N} f_i \quad (h=\Lambda/N) . \tag{B8}$$

Normally, the right-hand side would be an order $1/N^2$ approximation to the integral. Here, however, it is at least $O(1/N^6)$. This can be seen immediately via the *Euler-Maclaurin* summation formula [29,20]

$$\int_0^\Lambda dX\, f(X)=h\left[\tfrac{1}{2}(f_1+f_{N+1})+\sum_{i=2}^{N} f_i\right] - \frac{B_2 h^2}{2!}[f_X(\Lambda)-f_X(0)] - \frac{B_4 h^4}{4!}[f_{XXX}(\Lambda)-f_{XXX}(0)]$$
$$- \frac{B_6 h^6}{6!}[f_{XXXXX}(\Lambda)-f_{XXXXX}(0)]+O(1/N^8) , \tag{B9}$$

where the B_n's are Bernoulli numbers $(B_2/2!=\frac{1}{12}$, $B_4/4!=-\frac{1}{720}$, and $B_6/6!=\frac{1}{30240})$ [29]. Now because of the periodicity of the solutions to Eq. (A1), whose derivatives exist up to fourth order, the terms of orders h^2 and h^4 vanish on the right-hand side. If the solution is differentiable more often than four times, the trapezoidal rule (B8) becomes even more accurate. Apart from the prefactor h, the scalar product defined on the basis of the discretization (B8) and Eq. (B7) is identical to the ordinary scalar product in $\mathbb{R}^{2N}$. This prefactor does not play any role, because it affects both the orthonormalization step and the norm calculation—in effect we monitor only growth rates, not absolute magnitudes of vectors. Hence,

we can, after discretization, simply compute the scalar product of two vectors according to

$$\langle \mathbf{u}, \mathbf{v} \rangle = \sum_{i=1}^{2N} u_i v_i . \tag{B10}$$

We have tested our routine by recomputing known Lyapunov exponents of the Lorenz model, Rössler model, and Rössler hyperchaos [25,30]. Furthermore, we checked that an increase in the number of discretization points did not produce significant changes in the ex-

ponents obtained (except in two cases which are discussed in Sec. IV).

Note, finally, that a numerical estimate of a positive Lyapunov exponent cannot be improved indefinitely.

The reason is that roundoff errors will eventually render all trajectories periodic, which means that the numerical system is not chaotic on time scales beyond that limit. Hence the largest Lyapunov exponent will tend to zero.

[1] K. Kassner, C. Misbah, H. Müller-Krumbhaar, and A. Valance, preceding paper, Phys. Rev. E **49**, 5477 (1994).

[2] K. Kassner, C. Misbah, and H. Müller-Krumbhaar, Phys. Rev. Lett. **67**, 1551 (1991).

[3] A. Valance, K. Kassner, and C. Misbah, Phys. Rev. Lett. **69**, 1544 (1992).

[4] K. Brattkus and S. H. Davis, Phys. Rev. B **38**, 11452 (1988).

[5] Note that there is an error in the fourth linear term of Eq. (5.18) of Ref. [4]; this term should read $2k\nabla^2 H_0$.

[6] A. Ghazali and C. Misbah, Phys. Rev. A **46**, 5026 (1992).

[7] K. Kassner (unpublished).

[8] K. Kassner, *Pattern Formation in Diffusion-Limited Crystal Growth* (World Scientific, Singapore, in press).

[9] For one of the "workhorses" of the field, octylcyanobiphenyl (8 CB), $k \approx 0.9$ (see [10]).

[10] J.-M. Flesselles, A. J. Simon, and A. J. Libchaber, Adv. Phys. **40**, 1 (1991).

[11] C. Misbah, H. Müller-Krumbhaar, and D. E. Temkin, J. Phys. I **1**, 585 (1991).

[12] K. Sneppen, J. Krug, M. H. Jensen, C. Jayaprakash, and T. Bohr, Phys. Rev. A **46**, R7351 (1992).

[13] M. Kardar, G. Parisi, and Y. Zhang, Phys. Rev. Lett. **56**, 889 (1986).

[14] W. J. Boettinger, D. Shechtman, R. J. Schaefer, and F. S. Biancaniello, Metall. Trans. **15A**, 55 (1984).

[15] W. Kurz and R. Trivedi, Acta Metall. **38**, 1 (1990).

[16] M. Gremaud, M. Carrad, and W. Kurz, Acta Metall. **39**, 1431 (1991).

[17] A. Karma and A. Sarkissian, Phys. Rev. Lett. **68**, 2616 (1992).

[18] C. W. Gear, *Numerical Initial Value Problems in Ordinary Differential Equations* (Prentice-Hall, Englewood Cliffs, NJ, 1971).

[19] Occasionally, "strange" stationary solutions appeared, for example, a state consisting of two symmetric cells of different sizes. Substituting this solution into the dynamical code, we found it to be highly unstable; it decayed almost instantaneously into the asymmetric cell solution.

[20] W. H. Press, B. P. Flannery, S. A. Teukolsky, and W. T. Vetterling, *Numerical Recipes* (Cambridge University Press, Cambridge, 1986).

[21] T. S. Parker and L. O. Chua, *Practical Numerical Algorithms for Chaotic Systems* (Springer-Verlag, New York, 1989).

[22] Other than Poincaré maps defined in the vicinity of a known limit cycle (see Ref. [21]), the numerically more useful maps of the type described here need not be continuous.

[23] Time is measured in units of the renormalized diffusion time $\tau = l^2 / D\epsilon$.

[24] H. S. Greenside, A. Wolf, J. Swift, and T. Pignataro, Phys. Rev. A **25**, 3453 (1982).

[25] A. Wolf, J. B. Swift, H. L. Swinney, and J. A. Vastano, Physica D **16**, 285 (1985).

[26] H. Haken, Phys. Lett. **94A**, 71 (1983).

[27] Since our system depends on a continuous coordinate, N is infinite and even a spectrum of Lyapunov exponents possessing a continuous part is conceivable. However, as long as the motion is reducible to a few degrees of freedom, the largest exponents will form a discrete set. In practice, numerical discretization implies that we have to deal with finite N only.

[28] J. L. Kaplan and J. A. Yorke, *Chaotic Behavior of Multidimensional Difference Equations*, Lecture Notes in Mathematics (Springer, New York, 1979).

[29] *Handbook of Mathematical Functions*, edited by M. Abramowitz and I. Stegun (Dover, New York, 1972).

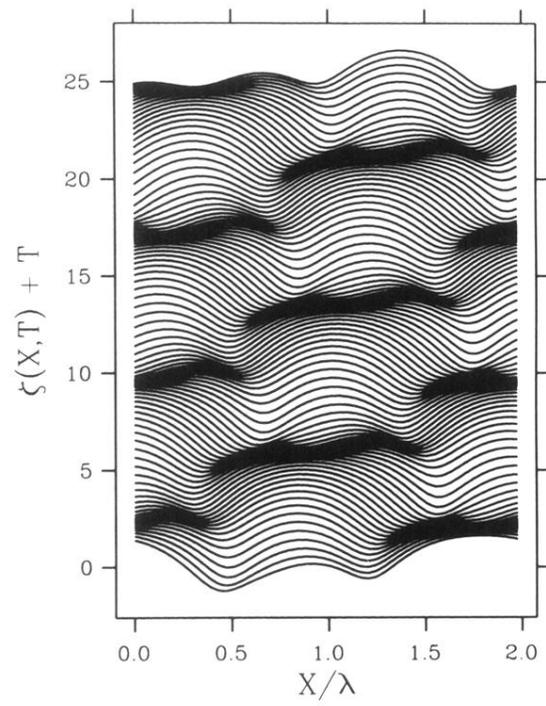[30] O. E. Rössler, Phys. Lett. **71A**, 155 (1979).

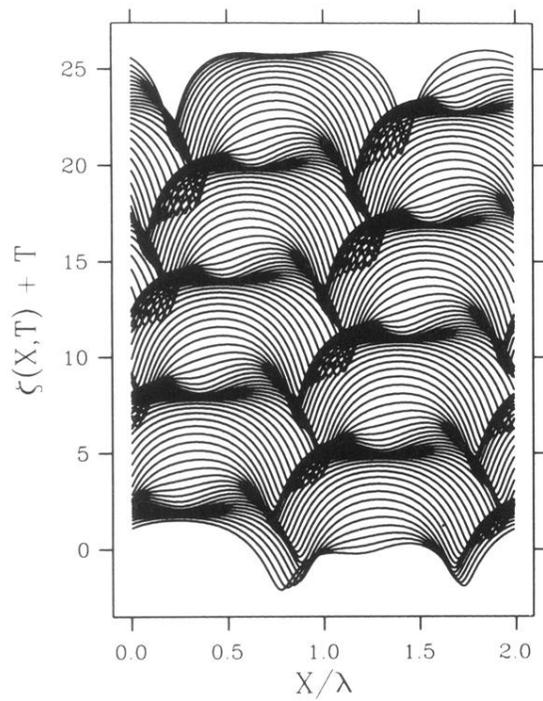FIG. 11. Space-time portrait of the time-period-doubling state of Figs. 9 and 10.

FIG. 14. A quasiperiodic state of the one-sided model. Parameters: $l_T^{-1} = 0.45$, $q = 1.0$, and $\nu = 0.0$.
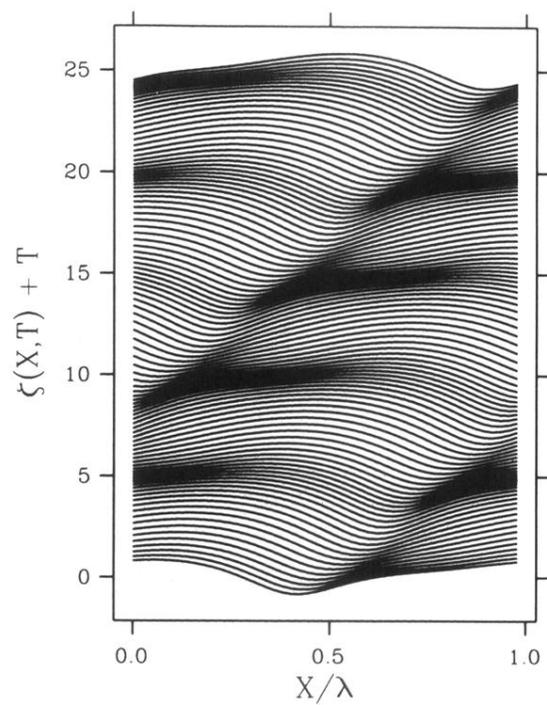
FIG. 16. Space-time portrait of quasiperiodic motion in scenario two. Parameters: $q = 0.753$, $l_T^{-1} = 0.28$, and $\nu = 1.0$.
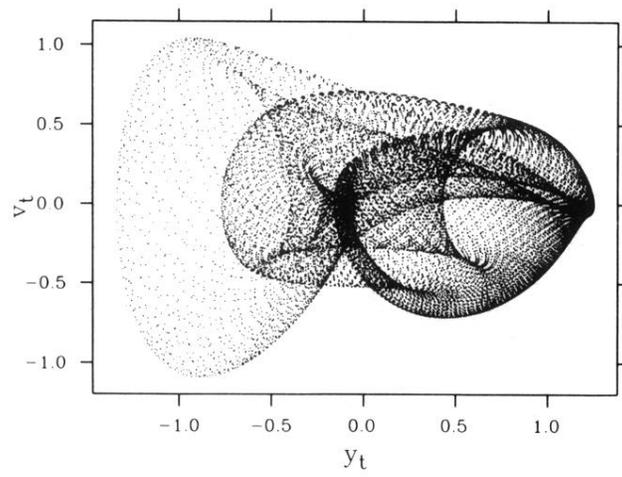
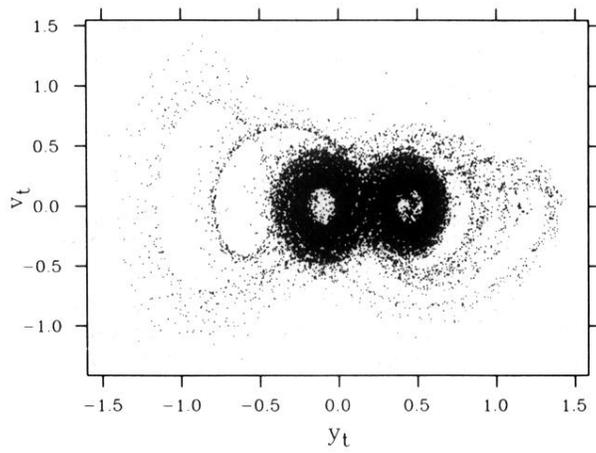FIG. 20. Stroboscopic map of the quasiperiodic state of Fig. 18.

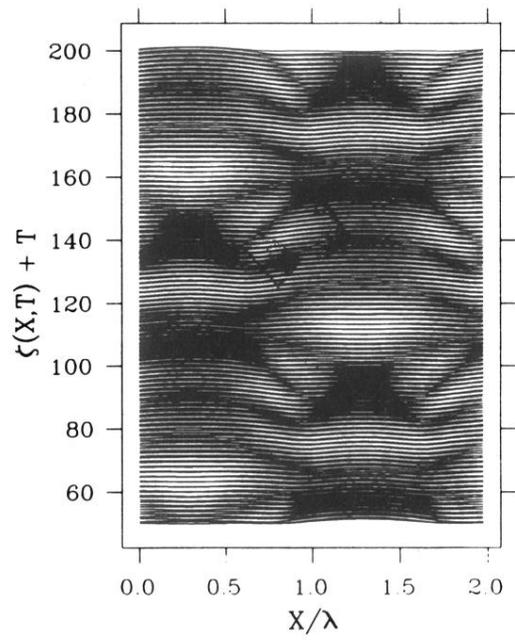FIG. 21. Stroboscopic map of the chaotic state of Fig. 19.

FIG. 22. Space-time portrait of a mode-locking state of order 5. Parameters: $l_T^{-1} = 0.256$, $q = 1.0$, and $\nu = 1.0$.
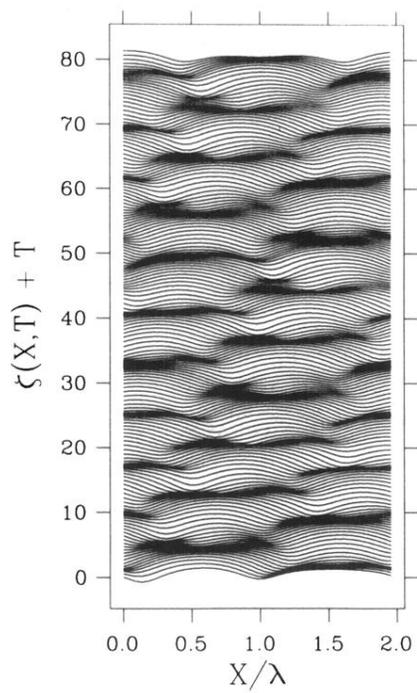
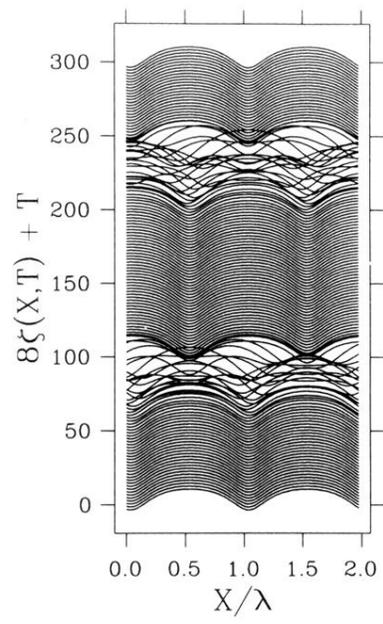FIG. 26. Space-time portrait of the state of Fig. 24.

FIG. 29. Space-time portrait of the interface dynamics of the state of Fig. 27. Here the interface height has been multiplied by eight for better visibility.
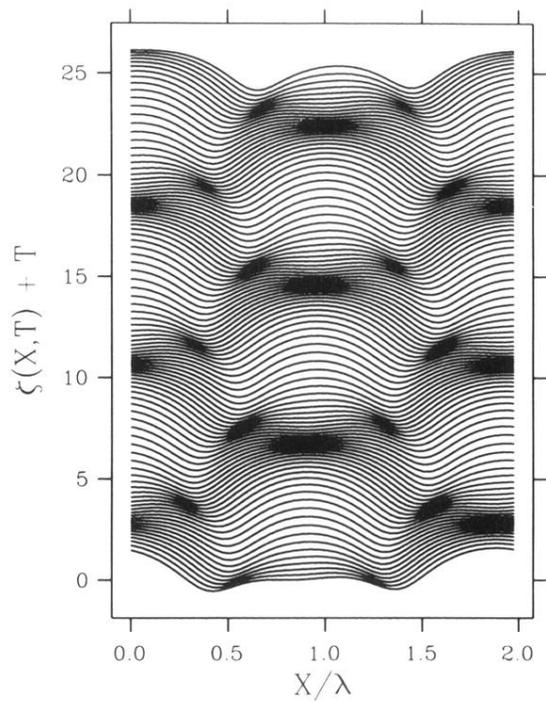
FIG. 6. Space-time portrait of quasiperiodic interface dynamics stemming from the superposition of drift and vacillating-breathing motions. The rules for these portraits are the same as in I, i.e., the y axis is a hybrid space-time coordinate, its units are the usual nondimensional ones; and the x axis is purely spatial, with units given by the wavelength of the basic symmetric solution, i.e., the largest x coordinate gives the aspect ratio. Parameters: $l_T^{-1} = 0.28$, $q = 0.9$, and $\nu = 1.0$.